



New geochemical constraints on the Paleocene–Eocene thermal maximum: Dababiya GSSP, Egypt



Hassan Khozyem^{a,b,*}, Thierry Adatte^b, Jorge E. Spangenberg^c, Gerta Keller^d, Abdel Aziz Tantawy^a, Alexey Ulianov^b

^a Department of Geology, Faculty of Sciences, Aswan University, Aswan, Egypt

^b Institute of Earth Sciences (ISTE), University of Lausanne, 1015 Lausanne, Switzerland

^c Institute of Earth Surface Dynamics (IDYST), University of Lausanne, Switzerland, 1015 Lausanne, Switzerland

^d Department of Geosciences, Princeton University, Guyot Hall, Princeton, NJ 08544, USA

ARTICLE INFO

Article history:

Received 11 June 2014

Received in revised form 21 March 2015

Accepted 6 April 2015

Available online 16 April 2015

Keywords:

Dababiya GSSP

Egypt

Geochemical proxies

Luxor

Mineralogy

PETM

ABSTRACT

The Paleocene–Eocene Thermal Maximum (PETM) shows an extraordinary drop in the $\delta^{13}\text{C}$ of carbonate and organic matter across the globe, suggesting massive release of ^{13}C -depleted carbon dioxide into the ocean and atmosphere over a very short time interval (probably <20ky). We report a geochemical and mineralogical study of 106 samples spanning the most expanded PETM at the Dababiya Global Stratotype Standard section and Point (GSSP) near Luxor, Egypt. The field and laboratory observations reveal that the deposition occurred in a submarine channel extended laterally about 200 m with the deepest part (~0.88 m) at the designated GSSP, although all bio-zones are present. Stable isotope records of both carbonate and organic carbon show decreases starting 0.6 m below the Paleocene–Eocene boundary (PEB) and culminating at the erosion surface. A persistent shift in $\delta^{15}\text{N}_{\text{org}}$ values to near zero reflects a gradual increase in bacterial activity. High Ti, K and Zr and low Si contents at the PEB coincide with increased kaolinite contents, which suggests intense chemical weathering under more humid conditions at the PETM onset. Two negative Ce-anomalies indicate intervals of anoxic conditions during the lower and middle PETM (base and top of zone E1). The first anoxic event is represented by a negative Ce-anomaly, high V/C and V/V + Ni ratios, negative Mn* and an abundance of idiomorphic pyrite crystals that indicate anoxic to euxinic conditions. The anoxic event (middle PETM) is marked by high U, Mo, V, Fe and abundant small sized (2–5 μm) pyrite framboids, increased Cu, Ni, and Cd at the same level suggesting anoxic conditions linked to high surface water productivity. Above this interval, oxic conditions returned as indicated by the precipitation of phosphorus and barium. These data reveal an expanded PETM interval marked by intense weathering as a crucial parameter during the recovery phase.

© 2015 Elsevier B.V. All rights reserved.

1. Introduction

The Paleocene–Eocene boundary (PEB) took place ca. 55.8 ± 0.2 Ma ago (Westerhold et al., 2009) associated with a sudden increase in Earth surface and deep ocean temperatures and an abrupt negative shift in the stable carbon isotope ratio ($\delta^{13}\text{C}$) of carbon-bearing phases. This abrupt global warming, known as the Paleocene–Eocene Thermal Maximum (PETM), was related to a rapid and massive release of ^{13}C -depleted CO_2 into the ocean, atmosphere or both (Dickens et al., 1995). The nature and tempo of the resulting $\delta^{13}\text{C}$ excursion is recorded from carbonate as well as marine and terrestrially derived organic matter (McInerney and Wing, 2011). The excursion is commonly interpreted as widespread release of methane from continental margins upon thermal dissociation of clathrates (Dickens et al., 1995). Solid clathrates,

comprised of ^{13}C -depleted methane and water, can occur in deep-sea sediments where methane concentrations exceed those on an equilibrium curve defined by pressure and temperature.

Therefore, with a major increase in deep-ocean temperature large quantities of methane might escape the seafloor, which would be rapidly oxidized to CO_2 in the water column or atmosphere. However, this type of methane release alone is probably insufficient to explain the huge CO_2 input into oceans and atmosphere during the Paleocene–Eocene (P–E) transition (Dickens et al., 1995; Zachos et al., 2004). Other explanations for the carbon input have been offered, including: (1) Pore fluid venting probably associated with gas hydrate dissociation and oxidation of organic matter-rich terrigenous sediments that increase the quantity of released greenhouse gases but remain insufficient to raise global temperature (DeConto et al., 2010). (2) Higgins and Schrag (2006) estimated that the oxidation of ca. 5000 Gt. of organic carbon most likely explains the geochemical and climatic changes during the PETM. The interaction of hydrothermal fluid with organic-rich Cretaceous–Paleocene sediments of the North Atlantic could

* Corresponding author at: Department of Geology, Faculty of Sciences, Aswan University, Aswan, Egypt.

E-mail address: [hkhoyem@gmail.com](mailto:hkhozyem@gmail.com) (H. Khozyem).

produce significant amounts of thermogenic methane (Svensen et al., 2004, 2010; Westerhold et al., 2009). And (3) desiccation and oxidation of organic matter in vast areas of dried epicontinental seas could have contributed a significant CO₂ input to the atmosphere (Gavrilov et al., 2003; Higgins and Schrag, 2006).

Whatever the source, the massive input of greenhouse gases was related to a global temperature rise of 5–9 °C during a period of about 200 ka (Sluijs et al., 2006; Zachos et al., 2006; Weijers et al., 2007; Handley et al., 2008). The environmental perturbations associated with the global temperature rise, such as increasing sea water salinity and drop in pH and dissolved oxygen, were the main reason for the 35–50% species extinctions in deep benthic foraminifera and diversification in marine planktic foraminifera (e.g., Lu et al., 1998; Alegret et al., 2009). The termination of the PETM crisis may be linked to increased marine and terrestrial biological productivity, which results in draw-down of atmospheric CO₂ (Bains et al., 2000; Torfstein et al., 2010). Silicate weathering is another mechanism for atmospheric CO₂ removal although operating at much lower rates than previously supposed (Kelly et al., 1996, 2005).

A continuous sedimentary record across the PETM is imperative to understand the nature and tempo of this event. A number of recent studies that explored the PETM at the Dababiya GSSP (Luxor, Egypt) mainly concentrated on the faunal response (e.g., Dupuis et al., 2003; Ernst et al., 2006; Aubry et al., 2007) and only a few petrographic and geochemical studies have been conducted (Soliman et al., 2006; Schulte et al., 2011, 2013; Khozyem et al., 2014). The characteristics of the Dababiya GSSP include the relatively gradual onset of the CIE, the presence of a basal phyllosilicate-rich interval devoid of calcium carbonate and overlain by an organic matter-rich interval, the development of anoxia and increased burial efficiency of organic carbon by reduced water column oxygenation (Schulte et al., 2011). This sedimentary sequence was deposited in an outer-shelf marine environment.

The main objective of this study is to gain further insights into paleoenvironmental and paleoclimatic changes across the PETM based on multi-disciplinary mineralogical and geochemical studies of the Dababiya GSSP. Understanding the GSSP, chosen for its complete and representative record, is critical as it forms the basis for comparison of PE boundary sequences worldwide. To this end we document the geochemical and climatic records of the GSSP, examine environmental responses to rapid warming in a low-latitude continental shelf setting and compare the results with published global records. Specific objectives include: (i) evaluation of PETM's stratigraphic completeness and potential for regional and global correlation; (ii) determining the nature, tempo and timing of the PETM; and (iii) evaluation of characteristic PETM signals in detrital and nutrient fluxes and consequently redox conditions.

2. Studied sections

2.1. Location

The Dababiya GSSP is located at the eastern side of the upper Nile Valley 35 km southeast of Luxor City (25°30'N, 32°31'E; Fig. 1, Dupuis et al., 2003; khozyem et al., 2014). Although a number of studies have concentrated on outcrops in the Dababiya area (Dupuis et al., 2003; Schulte et al., 2011, 2013), the GSSP section was never before sampled systematically. The reason is highly restricted access because of the limited outcrop exposure and fear that sampling would deplete the section. As a result permission for sampling the GSSP was routinely denied. We obtained permission by proposing to leave the GSSP in tact and instead sample one stratigraphic sequence 25 m to the east (Dababiya E) of the GSSP exposure and the other 50 m northwest (Dababiya NW, Fig. 1). This sampling strategy is advantageous because the GSSP is in the deepest part of a submarine channel with variable erosion on either

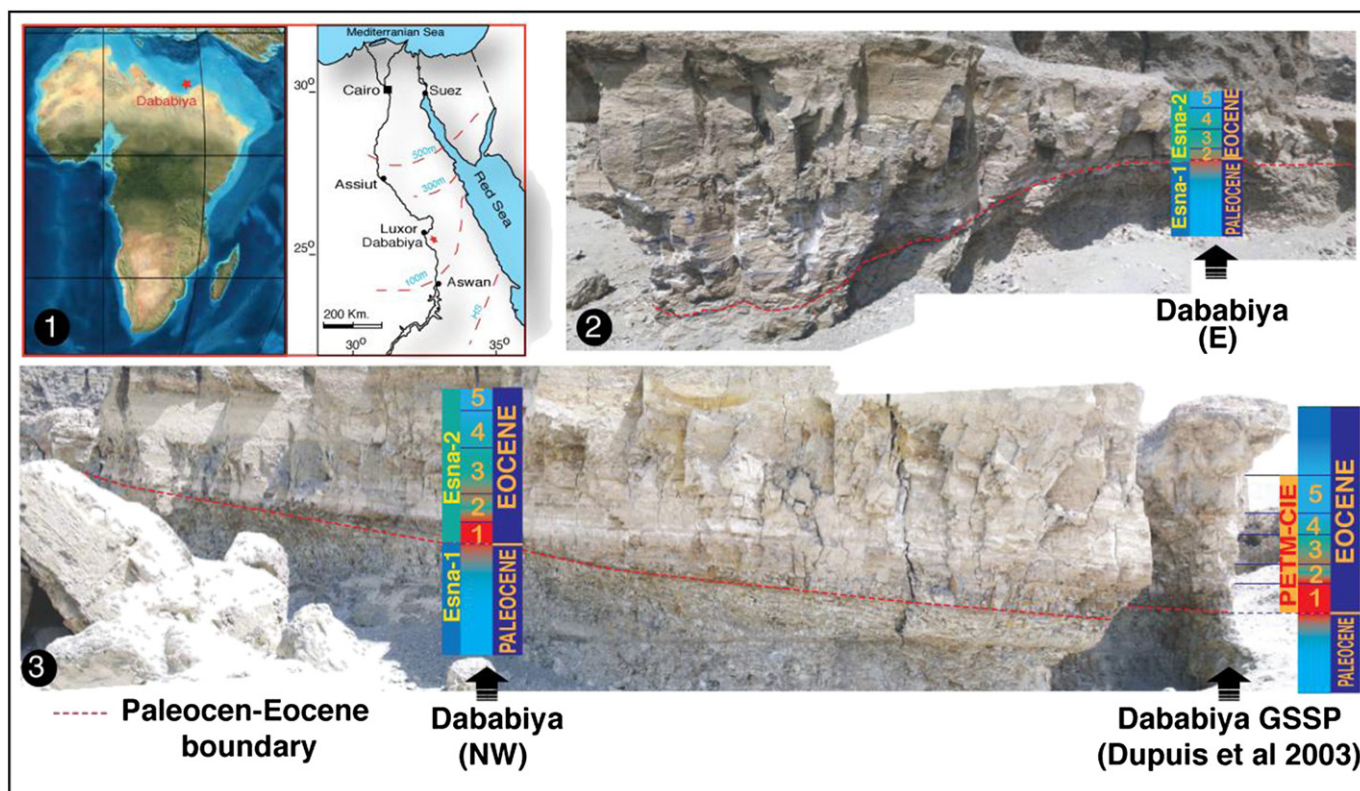


Fig. 1. A.1) Paleogeographic location (modified after Blakey, 2007) and present location of the Dababiya GSSP (modified from Dupuis et al., 2003). A.2 and A.3 show field photographs of the relative distance between NW and E sections at the main GSSP outcrop.

side. The two sections sampled ensure that the maximum available sediment deposition and variation in erosion and depositional patterns through the channel can be evaluated and compared with the already published GSSP record (Dupuis et al., 2003).

2.2. Paleodeposition and lithostratigraphy

The Paleocene-Eocene transition in the southern margin of the Tethys in Egypt includes the outer-shelf deposits of northeastern Egypt and Sinai (i.e. Wadi Nukhul, Speijer and Wagner, 2002; Khozyem et al., 2013). In the eastern desert the monocline of the Upper Cretaceous to Upper Eocene resulted in uplift and exposure of the outer shelf to marginal marine strata across the desert in northeastern Egypt where they are exposed in mesas and ridges (Aubry et al., 2007). The Dababiya GSSP is one of these exposures. Exposures in the Dababiya area consist of four lithostratigraphic formations as follows from older to younger (Fig. 2): Dakhla Shale Formation (greenish calcareous shale), Tarawan Formation (marly limestone to chalk), Esna Shale (greenish gray to dark gray shale), and the Thebes Formation (limestone and flint). The Esna Shale Formation is divided into three main units (Esna-1, Esna-2 and Esna-3) based on carbonate contents (Dupuis et al., 2003). Only Esna-1 and Esna-2 are exposed at the GSSP NW and E outcrops (Fig. 1, 2).

The Paleocene-Eocene boundary (PEB) is in the lower part of the Esna shale Formation between units Esna-1 and Esna-2. Esna-1 consists of marl to marly shale. A well-defined erosional sequence boundary (SB) separates Esna-1 and Esna-2 (Fig. 2). The lithology of the overlying Esna-2 unit is divided into five lithologically distinct beds that comprise the PETM interval (Dupuis et al., 2003). The thickness and lithologies of these beds varies laterally across the submarine channel as seen in the litho-columns of the GSSP (Schulte et al., 2011; Khozyem et al., 2014), as well as NW and E outcrops (Fig. 2). In the field, the PEB is marked by the lithologic change from marl or marly shale (Esna-1) to laminated clay with few phosphatic coprolites but devoid of carbonate in the overlying Bed-1. Bed-2 consists of brown shale with carbonate content at the GSSP, but in NW and E outcrops silty claystone with anhydrite layers predominate. In Bed-3 laminated phosphatic shale dominate the GSSP and silty marl with phosphatic nodules and anhydrite mark the NW

and E outcrops similar to Bed-2. Upwards in the section carbonate content increases from gray shale to marly limestone in Bed-4 and to gray marl and calcarenitic limestone in Bed-5. This lateral variation reflects deposition within the deepest part of the submarine channel (GSSP) and to the channel banks on either sides (NW and E sections).

3. Material and methods

3.1. Sample preparation

In the field, vertical outcrops of the Dababiya NW and E sections were sampled at high sample resolution of 2, 5 and 10 cm from the Upper Paleocene to Lower Eocene (Fig. 2). In the laboratory, the surface of each sample was carefully cleaned and all weathered material removed. An aliquot of ca. 25 g was powdered in a washed and air-dried agate mortar (washed three times with deionized water and once with ethanol). The samples were subjected to extensive mineralogical and geochemical studies at the Institute of Earth Sciences, University of Lausanne, Switzerland.

3.2. XRD mineralogy

Whole rock mineralogical composition was performed using a X-TRA Thermo-ARL Diffractometer, following the procedure described in Klug and Alexander (1974), Kübler (1987); Adatte et al. (1996). This method for semi-quantitative analysis of the bulk rock mineralogy (obtained by XRD patterns of random powder samples) uses external standards with error margins varying between 5 and 10% for the phyllosilicate and 5% for grain minerals. A detrital index (DI) was calculated as the ratio between calcite content and the sum of detrital minerals ($DI = \text{Calcite} / (\text{Quartz} + \text{Phyllosilicates} + \text{Plagioclases} + \text{K-Feldspars})$).

Clay mineral XRD analysis was done using a X-TRA Thermo-ARL Diffractometer, following the procedure described in Kübler (1987); Adatte et al. (1996). Samples are introduced into glass containers with deionized water, then decarbonized by HCl 10% (1.25 N) during 20 minutes and regularly agitated. Dissolution is helped by 3 minutes of ultrasonic disaggregation for each sample. The insoluble residues

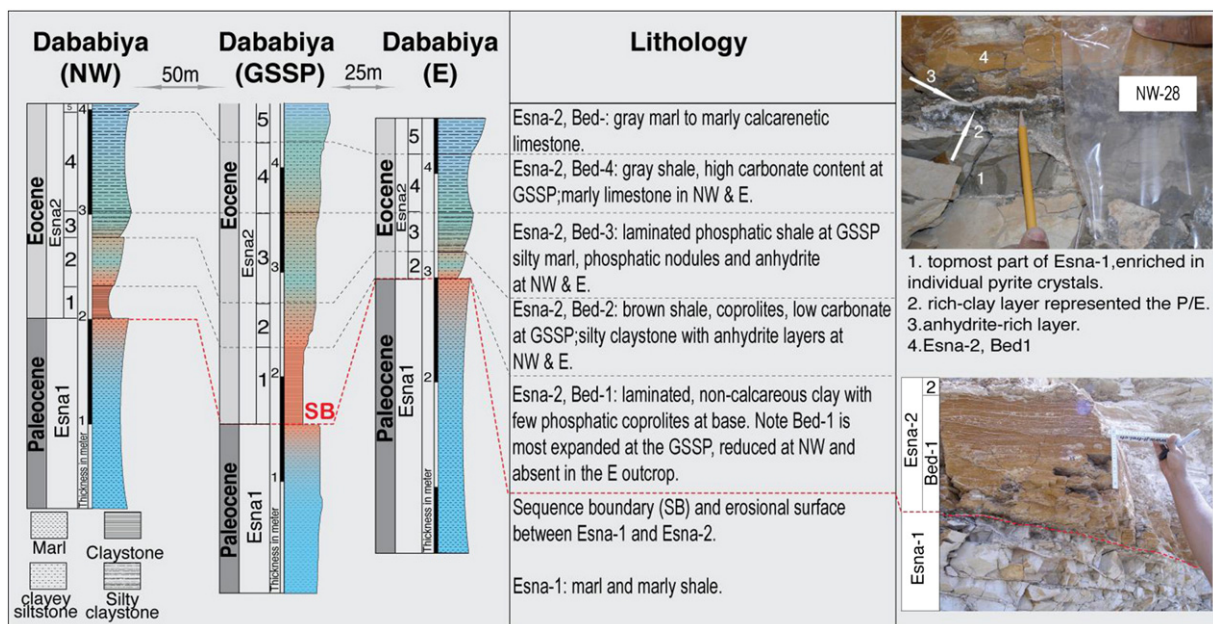


Fig. 2. Lithology and description of the NW and E sections correlated with the GSSP; field photograph focuses on the P/E boundary and the contact between Esna-1 and Esna-2. Note the presence of a continuous layer of anhydrite is located 2 cm above the PEB.

are washed by centrifugation and repeated until a neutral solution (pH 7) is obtained. Following the Stokes law, two granulometric fractions (<2 µm and 2–16 µm) are pipetted and deposited on a glass plate. After air-drying, samples are analyzed by XRD. Subsequently, the <2 µm fraction samples are saturated with ethylen-glycol and re-measured in order to check for swelling minerals. This method allows the semi-quantification of the proportion of clay minerals with a precision better than 5%.

3.3. SEM

Selected samples close to the PETM interval were studied by scanning electron microscopy (SEM; Tescan Mira LMU) after gold-carbon coating.

3.4. Isotopes

Carbon and oxygen isotope analyses of aliquots of whole rock samples were performed using a Thermo Fisher Scientific Gas Bench II carbonate preparation device connected to a Delta Plus XL isotope ratio mass spectrometer. The CO₂ extraction was done by reaction with anhydrous phosphoric acid at 90 °C. The standardization of the δ¹³C and δ¹⁸O values relative to the international VPDB scale was done by calibration of the reference gases and working standards with IAEA standards. Analytical uncertainty (1 σ), monitored by replicate analyses of the international calcite standard NBS-19 and the laboratory standards Carrara Marble was not greater than ±0.05‰ for δ¹³C and ±0.1‰ for δ¹⁸O.

Organic matter was separated from the samples by HCl treatment, dried (40 °C, 16 h), and subjected to carbon and nitrogen isotope analysis by flash combustion on a Carlo Erba 1108 elemental analyzer connected to a Thermo Fisher Scientific Delta V isotope ratio mass spectrometer that was operated in the continuous helium flow mode via a ConFlo III split interface. The δ¹³C and δ¹⁵N values were reported relative to VPDB and air–N₂, respectively. The calibration and assessment of the reproducibility and accuracy of the isotopic analysis were based on replicate analyses of laboratory standard materials and international reference materials. The reproducibility was better than 0.1‰ (1 σ) for both carbon and nitrogen.

3.5. Major, trace and rare earth elements

Major elements (ME) were analysed by XRF on lithium tetraborate glass discs using a Philips PW2400 X-ray fluorescence spectrometer. These data were complemented by the determination of selected trace elements (TE) on pressed powdered discs with a Mowiol II polyvinyl alcohol matrix, using the same XRF spectrometer as for the major element analysis. Detection limits approached 0.01% (ME) and 1–4 ppm (TE). Accuracy was assessed by the analysis of certified reference materials.

The rare earth element (REE) and further trace element data were obtained by laser ablation inductively coupled plasma mass spectrometry (LA–ICPMS). A GeoLas 200M 193 nm excimer ablation system interfaced to an Elan 6100 DRC quadrupole ICPMS was used for the ablation of the lithium tetraborate discs previously analysed by XRF. The ablation system was operated at a beam size of 120 µm, repetition rate of 10 Hz and on-sample energy density of ~10 J/cm². Helium was used as a carrier gas. The relative sensitivity factors were calibrated using a NIST SRM 612 standard representing a soda-lime-silica glass doped with trace elements. Calcium contents by XRF were used for internal standardisation. Accuracy was typically better than 5%. Detection limits ranged from 0.02 to 0.15 ppm (REE).

3.6. Total organic matter (TOC)

Organic matter contents were determined using Rock Eval pyrolysis (Rock-EvalTM6 Behar et al., 2001). The TOC values were obtained using

the standard temperature cycle. Samples were calibrated with both IFP160000 and an internal standard with an instrumental precision of <2% (Espitalié et al., 1985).

3.7. Biostratigraphy

For foraminiferal analysis, about 100gr. sediment was processed per sample by standard methods and washed through 63 µm and 38 µm screens to preserve small species (Keller et al., 1995). Biostratigraphic analysis was performed on >63 µm and 38–63 µm size fractions. Quantitative counts of ~300 specimens were picked from the >63 µm size fraction, mounted on cardboard slides for a permanent record and identified to obtain relative species abundance data. The remaining sample residue for each sample was searched for rare and zone-defining index species. For calcareous nannofossils, samples were processed at Aswan University, Aswan, Egypt, based on smear slide preparation from raw sediment samples as described by Perch-Nielsen (1985). The calcareous nannofossils were observed under the light microscope at a magnification of 1000x. The taxonomy used is described in Aubry et al. (1999); Perch-Nielsen (1985).

4. Results

4.1. Biostratigraphy and age constraints

The Dababiya Quarry Paleocene-Eocene boundary GSSP was selected by the International Commission for Stratigraphy (ICS) based on the following criteria: (1) the global δ¹³C_{org} and δ¹³C_{carb} isotope excursions (CIE), (2) disappearance of the deep water benthic foraminifer *Stensioina beccariiiformis*, (3) transient occurrence of planktonic foraminifera (*Acarinina africana*, *A. sibaiyaensis*, *Morozovella allisonensis*) during the δ¹³C excursions, (4) transient occurrence of the *Rhombaster* spp. – *Discoaster araneus* assemblage and (5) acme of the dinoflagellate *Apectodinium* (Aubry et al., 2007). Although a number of studies have investigated the PEB transition in the Dababiya Quarry area (e.g., Berggren and Ouda, 2003; Dupuis et al., 2003; Alegret et al., 2005; Alegret and Ortiz, 2006), the actual GSSP outcrop has rarely been sampled and analyzed.

4.1.1. Planktic foraminifera

The biostratigraphy for the Dababiya NW outcrop in this study is based on high-resolution planktic foraminifera and calcareous nannofossils (Fig. 3). Planktic foraminifera span biozones P4c, P5, E1 and E2 with an estimated time span of 2 m.y. (54.5–56.5 Ma, Olsson et al., 1999; Pearson et al., 2006). Zone P4c marks the base of the section as indicated by the disappearance of the index species *Globanomalina pseudomenardii*. This assemblage is dominated by *Igorina tadjikistanensis*, *Acarinina soldadoensis*, *Subbotina hornibrooki*, *Morozovella acuta* and *M. aequa*. The interval from the extinction of *Gl. pseudomenardii* to the first appearance of *Acarinina sibaiyaensis* defines zone P5 and the top of the Paleocene. At Dababiya NW this interval marks the onset of the PETM event with a 40% increase in species diversity (from 21 to 35 species) and decreased abundance of the dominant zone P5 species correlative with a gradual decrease in δ¹³C_{org} and δ¹³C_{carb} values that culminates at the PEB (Fig. 3).

Zone E1 above the PEB is a 42 cm thick barren clay interval (Bed-1). A 5 cm thick interval above E1 contains a good assemblage of the transient PETM fauna dominated by *A. sibaiyaensis* and *A. africana* and the first appearances of *A. africana*, *Morozovella allisonensis*, and the base zone E2 index species *Pseudohastigerina wilcoxensis*. Foraminifera are rare in the 35 cm spanning the upper Bed-2 and Bed-3 (upper part of PETM) but a diverse and well-preserved zone E2 assemblage returns in Bed-4. The return of this thriving assemblage coincides with the recovery of the δ¹³C_{org} and δ¹³C_{carb} values after the PETM.

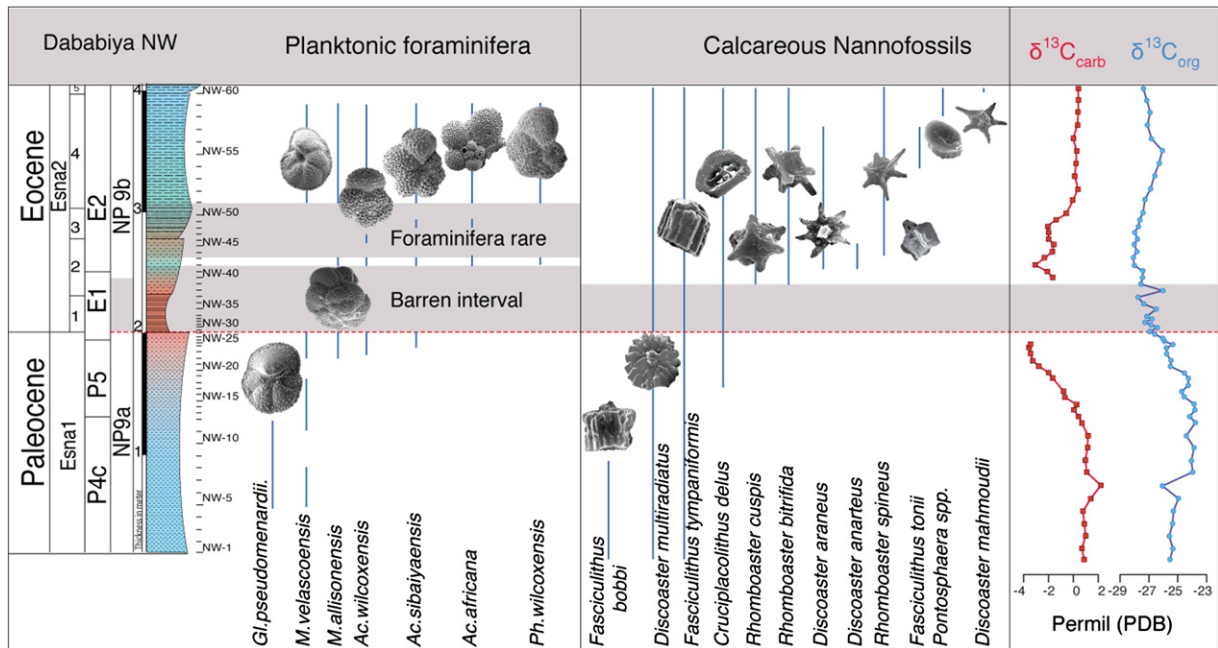


Fig. 3. Carbon isotopes ($\delta^{13}\text{C}_{\text{org}}$ and $\delta^{13}\text{C}_{\text{carb}}$) and selected ranges of planktic foraminifera and calcareous nannofossil species from the NW section located at 50 m to the left of the Dababiya GSSP. Note that a reduction in species richness in the late Paleocene is offset by a few new species during the gradual decrease in carbon isotopes and this evolutionary trend increased during the gradual recovery in carbon isotopes in the early Eocene (modified from Khozyem et al., 2014).

4.1.2. Calcareous nannofossils

Calcareous nannofossils at Dababiya span biozones NP9a (upper Paleocene) and NP9b (lower Eocene). Assemblages are moderately diversified (Fig. 3), preservation varies from poor to moderate, and except for the dissolution interval that spans Bed-1 and the lower part of Bed-2. Below the barren interval, nannofossil diversity averages about 16 species, whereas above it both abundance and diversity sharply decrease to about 8 species and dissolution resistant taxa dominate (e.g. *Discoaster* spp., *Coccolithus pelagicus*) along with reworked forms. Nannofossil diversity increases gradually and reaches a maximum at the base of Bed-5.

Most species of zone NP9a disappear at the P/E transition, and only *Fasciculithus tympaniformis* survived into the lowermost Eocene. The presence of this species along with *Fasciculithus tonii* in the upper part of Dababiya NW (Bed-4) is likely reworked, as they are known to disappear at the PETM onset (e.g., Monechi et al., 2000; Raffi et al., 2005; Tantawy, 2006; Agnini et al., 2007). The NP9a/NP9b transition coincides with the PETM dissolution interval, which is followed by the first appearance of *Rhomboaster cuspid* and *R. bitrifida*, *D. araneus* and *D. anartus*, whereas *C. eodelus* appears earlier in NP9a and *R. spineus* later in NP9b similar to the southeast Atlantic (Agnini et al., 2007) and Kharga Oasis, Western Desert, Egypt (Tantawy, 2006).

4.2. Whole rock and clay mineralogy

4.2.1. Whole rock mineralogy

At Dababiya NW, upper Paleocene sediments (zones P4c–P5) consist of typical marls (average 42.7% calcite, 40.7% phyllosilicates, 7% quartz, 0.4% anhydrite, absence of Ca-apatite; DI ~ 1.1, Fig. 4A). Near the PEB, a sharp decrease in calcite content to 5.4% coincides with rapidly increasing phyllosilicates (57.7%), quartz (8.2%), anhydrite (7.1%), Ca-apatite (7.5%) and presence of goethite, K and Na feldspar (DI ~ 0).

The interval between the PEB and 1.1 m above, zone E1 to base E2, (Beds 1 to 3) is characterized by two major changes based on whole rock compositions. The lower part corresponding to zone E1 (samples NW29–NW39) is marked by an abrupt increase in phyllosilicates, quartz, goethite and anhydrite, DI ~ 0, presence K and Na feldspars,

and low calcite. The low Ca-apatite, probably derived from reworked underlying sediments or rare coprolites. Above this interval, at the zone E1/E2 boundary (samples NW40–NW50), is a sharp increase in calcite (34.5%), a concurrent increase in Ca-apatite (up 25.6%) and a relative increase in anhydrite. Marly sediments return in the top 1 m interval corresponding to the upper zone E2 (Bed-4 to 5, Fig. 4A).

At Dababiya E, whole rock compositions are similar to the NW section, although deposition is more condensed with Bed-1 and much of Bed-2 missing due to erosion and non-deposition (Fig. 4B). Upper Paleocene sediments are typical marls with 38.8% phyllosilicate, 5.34% quartz, and 49.7% calcite. At the PEB and sequence boundary (SB) phyllosilicate, quartz and Feldspar increase and calcite drops to near 0%. From Bed-2 to the upper part of Bed-3 (samples E-22 to 31) quartz (25.1%), phyllosilicate (9.3%) and calcite (35.3%) increased. Marly sediments return in the upper part of the section.

4.2.2. Clay mineralogy

The clay fraction of the Dababiya NW is composed of smectite, illite, kaolinite, chlorite, illite-smectite and palygorskite. Smectite is the major component below the PEB (mean value 68%), followed by 14% of illite, 6.5% illite-smectite, 3.9% palygorskite, 3.5% kaolinite, and 3.25% chlorite. At the PEB-SB, smectite increased (mean 75%, dark shading) with almost no change in the other components (Fig. 5). In the middle of Bed-2, (E1/E2 transition, NW39–44, light shading), a sudden decrease in smectite (45%) is concomitant with a sharp increase in kaolinite (up to 10%) and a gradual increase in illite (18.5%), chlorite (12%), illite-smectite (10.8%) and palygorskite (8.8%). Above sample NW-44, the clay composition returns to the mean composition observed below the PEB.

4.3. Stable isotopes

4.3.1. Inorganic carbon isotope

At Dababiya NW, the $\delta^{13}\text{C}_{\text{carb}}$ values show an expanded carbon isotope excursion with gradual onset and recovery (Fig. 6A). During the upper Paleocene, correlative with zone P4, $\delta^{13}\text{C}_{\text{carb}}$ values are relatively stable around 1‰ (samples NW1–12). In the uppermost Paleocene (zone P5, NW16–27) $\delta^{13}\text{C}$ values gradually decrease by 4‰ to reach minimum

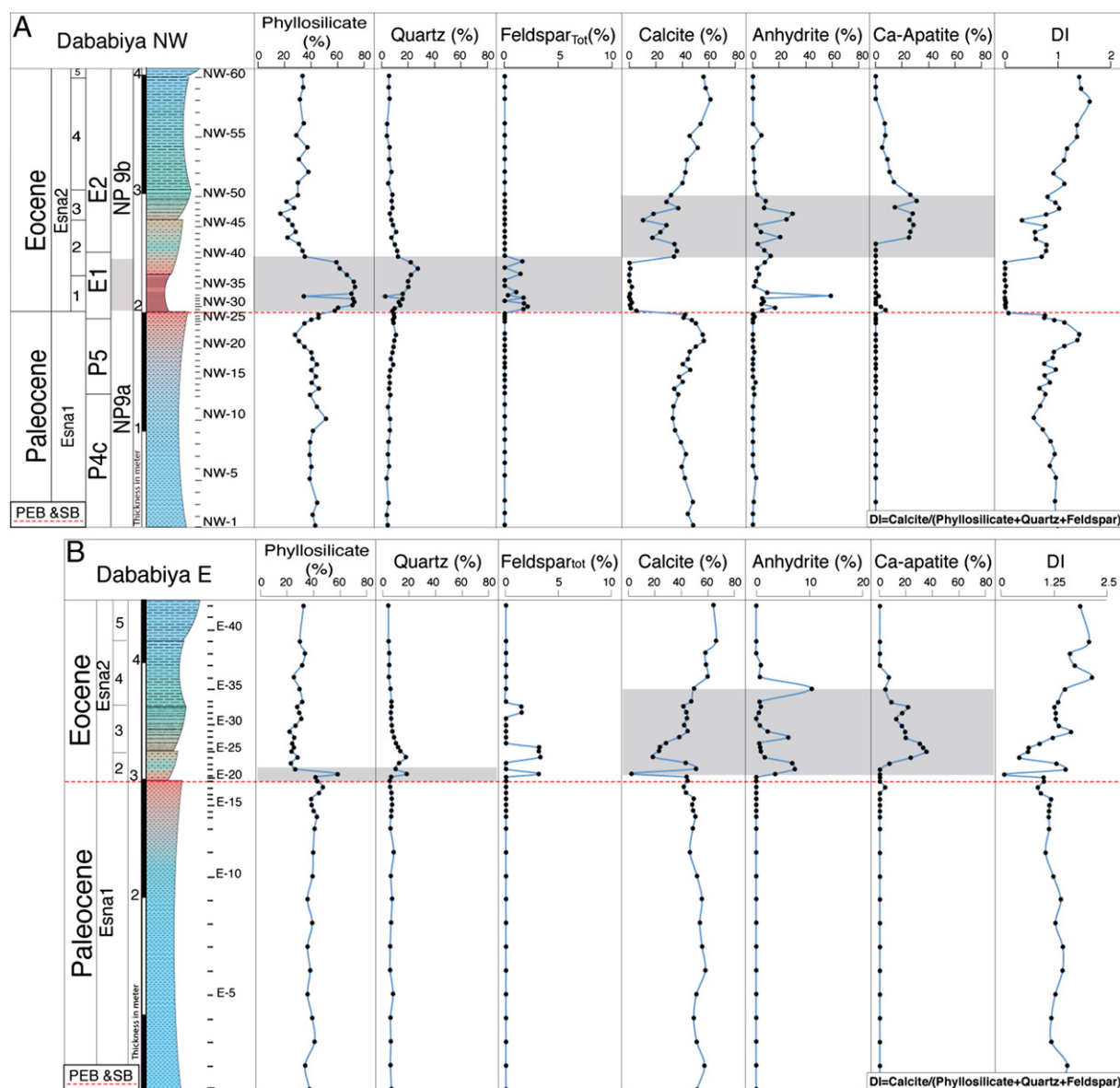


Fig. 4. A) Bulk rock compositions at the NW section. Note the increased phyllosilicate and quartz with the presence of feldspar in the first 50 cm above the sequence boundary (SB). Increase Ca-apatite coincides with increased calcite contents and several intervals enriched in anhydrite. B) Bulk rock composition at the E section. Note the increased calcite and Ca-apatite just above the SB indicates the absence (hiatus) of the uppermost Paleocene–lowermost Eocene. The gray shadow focuses on the interval where bulk rock components are increasing.

values about 20 cm below the PEB (Fig. 6A). The lower Eocene interval (zone E1) is devoid of carbonate. The initial recovery in the lower part of zone E2 (top of Bed-2) ranges between -2 to -3% . This is followed by a rapid increase across the Bed-3/Bed-4 boundary to 0.39% and remains relatively stable to the top of the section (Fig. 6A).

4.3.2. Organic carbon isotope

The $\delta^{13}\text{C}_{\text{org}}$ values show a similar pattern although the onset of the pre-PEB decrease is delayed relative to $\delta^{13}\text{C}_{\text{carb}}$. During the late Paleocene zones P4 to middle P5, $\delta^{13}\text{C}_{\text{org}}$ values gradually increase from -25.8 to -23.8% , then rapidly decrease across the PEB to reach minimum values in the upper part of Bed-2 (near base zone E2, Fig. 6A). In zone E2 $\delta^{13}\text{C}_{\text{org}}$ gradually increases but remains well below latest Paleocene values.

4.3.3. Nitrogen isotope

The $\delta^{15}\text{N}_{\text{org}}$ values show a similar trend as observed for $\delta^{13}\text{C}_{\text{carb}}$ and $\delta^{13}\text{C}_{\text{org}}$ across the PETM excursion at Dababiya NW. Maximum $\delta^{15}\text{N}$ values are recorded near the base of the section and the onset of the

negative shift is correlative with the onset in $\delta^{13}\text{C}_{\text{org}}$ (Fig. 6A). At the PEB $\delta^{15}\text{N}$ values drop to 6% and reach minimum values $\sim 2\%$ at the zone E1/E2 transition. A gradual increase through Bed-4 (zone E2) ends with a rapid increase to late Paleocene (zone P4) values at the top of the section.

At the Dababiya E section, the isotopic profiles record the same PETM excursions as at the NW section but the lower half is missing due to erosion at the SB (Fig. 6B). This is evident by the absence of the gradual decrease in isotope values at the Dababiya NW section, the sharp negative isotope shift at the PEB and SB erosion surface, the abrupt $\delta^{15}\text{N}_{\text{org}}$ drop, the missing Bed-1 and lower part of Bed-2. Similar to Dababiya NW, $\delta^{13}\text{C}_{\text{carb}}$ recovery begins in middle Bed-2 and $\delta^{13}\text{C}_{\text{org}}$ and $\delta^{15}\text{N}$ in Bed-3 followed by a gradual recovery into Bed-4 and return to pre-excursion values at the top of the section.

4.4. TOC contents

The TOC contents of the Dababiya NW section are generally low and highly degraded, as observed from the low hydrogen index (HI) and

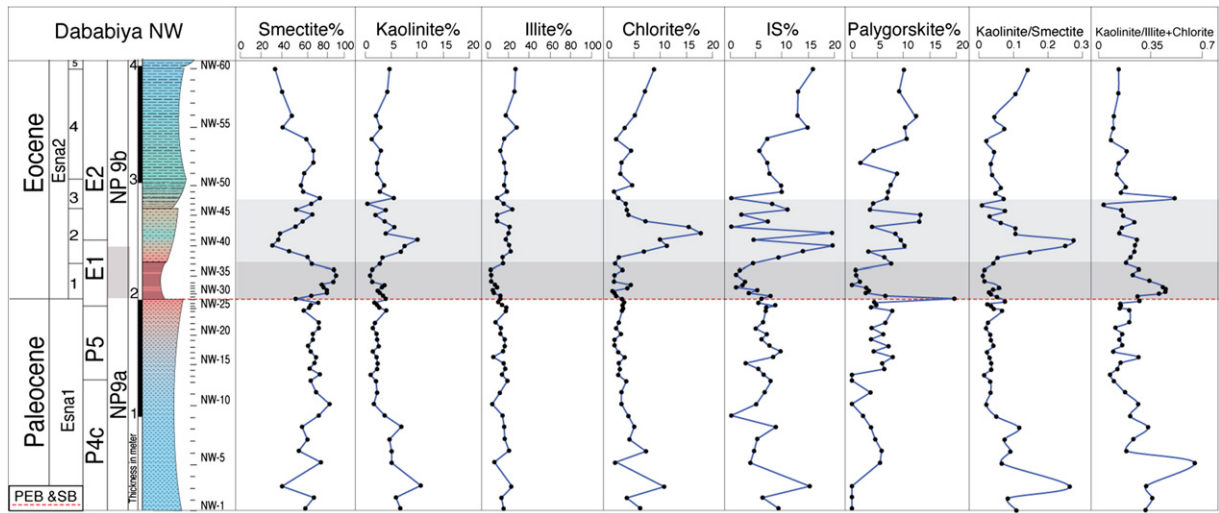


Fig. 5. Relative percent and ratios (kaolinite/smectite, kaolinite/illite + chlorite) of clay minerals in the NW section. Note, the increase in kaolinite, chlorite, IS, palygorskite to the detriment of smectite at 50 cm above the SB. The kaolinite/illite + chlorite ratio increases at the SB and then gradually decreases to the top of the PETM interval.

high oxygen index (OI) (Fig. 7). Below the PEB, the organic matter content ranges between 0.17 to 0.35% with the maximum value close to the PEB. From the PEB to sample NW37, the OM content decreased relative to values observed below the PEB (from 0.08 to 0.24%). TOC from sample NW38 to NW51 is enriched ranging between 0.59 to 1.32% with maximum concentrations from NW39 to NW42. TOC is mainly Type-III organic matter that reflects a continental source or highly weathered marine OM (Fig. 7). Above sample NW51, TOC content gradually decreases up to the top of the section with an average of 0.43%.

4.5. Geochemistry

4.5.1. Major elements

Major element abundances vary significantly in the Dababiya NW section and are mainly linked to variations in clay contents (Fig. 5, 8A). No significant changes in MEs are observed in the late Paleocene zone P4c (0–60 cm) of the section. In the interval up to the PEB–SB (zone P5) concentrations gradually decrease with mean values of 33%

SiO₂, 9.12% Al₂O₃, 0.36% TiO₂, 3.1% Fe₂O₃, 2% Na₂O₃, and 0.27% K₂O coincident with increased CaO (mean 22.56%). No notable changes are observed in this interval in MgO, MnO and P₂O₅ concentrations.

Above the PEB and SB to the base of Bed 2 all ME components abruptly change (mean values 52.5% SiO₂, 13% Al₂O₃, 0.75% TiO₂, 4.52% Fe₂O₃, 2.76% MgO, 3.37% Na₂O₃ and 1.02% K₂O). No changes are detected in P₂O₅ content but MnO and CaO decrease significantly to 0.01 and 4.28%, respectively. Above this interval, all MEs gradually return to the mean values observed below the PEB except for P₂O₅, which rapidly increased in Bed-3 (mean value 6.05%; samples NW41–51) and Fe₂O₃ remains high up to the top of Bed-2, Fig. 8A).

4.5.2. Trace elements

Trace element concentrations in marine sediments are commonly normalized by the Al-content to avoid dilution effects by carbonate. One uses reference materials when enrichment factors are calculated (Brumsack, 2006; Riquier et al., 2006; Tribouillard et al., 2006). At Dababiya NW, the Al-normalized trace elements trends are distinct

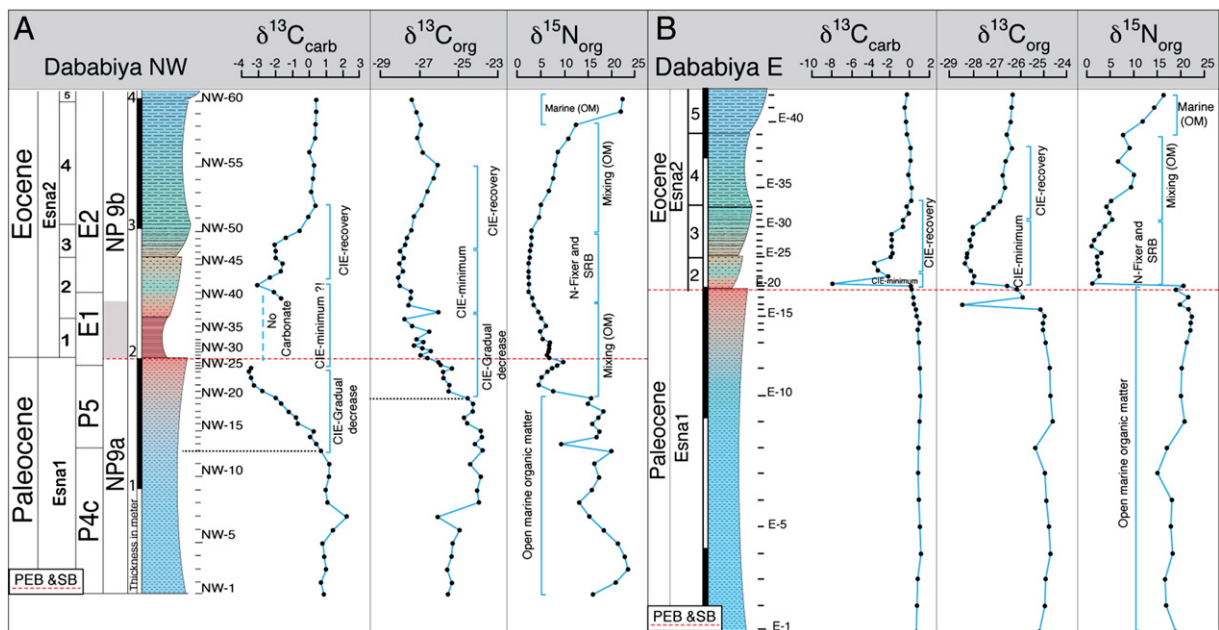


Fig. 6. $\delta^{13}\text{C}_{\text{carb}}$, $\delta^{13}\text{C}_{\text{org}}$ and $\delta^{15}\text{N}$ for the NW and E sections show: A) a gradual decrease in carbon isotopic composition of both $\delta^{13}\text{C}_{\text{carb}}$ and $\delta^{13}\text{C}_{\text{org}}$ at the NW section, starting below the PEB (60 cm for $\delta^{13}\text{C}_{\text{carb}}$ and 30 cm for $\delta^{13}\text{C}_{\text{org}}$ and $\delta^{15}\text{N}$); B) an abrupt shift in $\delta^{13}\text{C}_{\text{carb}}$ and $\delta^{13}\text{C}_{\text{org}}$ and $\delta^{15}\text{N}$ in the E sections starting at the PEB.

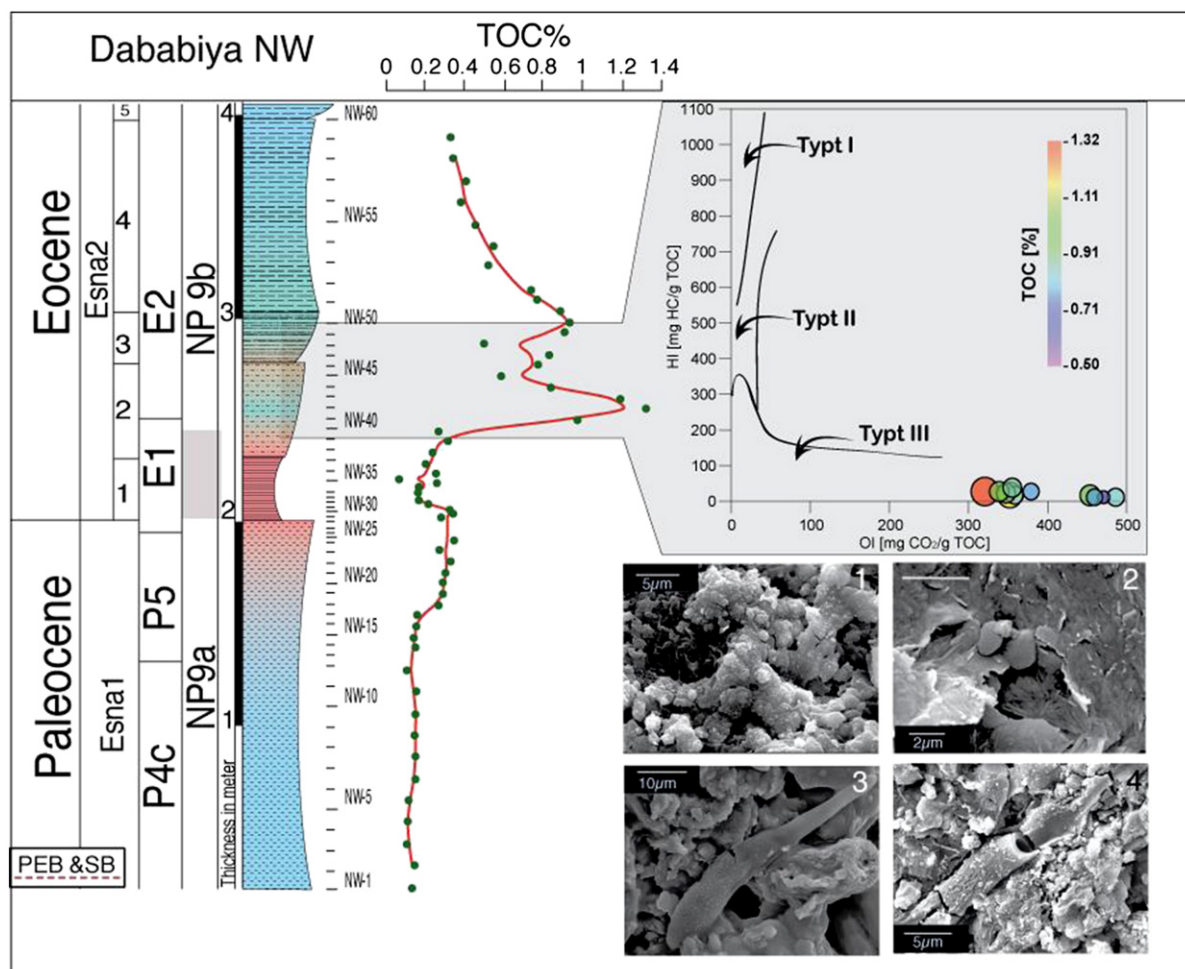


Fig. 7. Total organic contents (TOC) in percent show increasing organic matter in the interval between NW38 and NW49 whereas HI and OI cross plot shows the terrestrial origin of the organic matter. SEM micrographs represents examples of different organic matter debris from the second anoxic interval at Dababiya NW. The organic matter debris includes different fragments of higher plants thought to be from terrestrial sources.

across the PETM interval (Fig. 8B). At the E1/E2 zone boundary (middle Bed-2, NW38–42, shaded) V, U, Mo, Cd, Ni, and Zn are strongly enriched then abruptly drop to pre-excursion values of basal Eocene zone E1, Bed-1 and late Paleocene. Al-normalized Cu, Zr and Pb are enriched above the PEB in zone E1 (Bed-1 to middle Bed-2) and rapidly return to pre-PEB values. In contrast, Co/Al and Ba/Al show minimum values in Bed-1 and Co/Al increased gradually above Bed-1 to the top of the section (Fig. 8B). Cr/Al concentrations broadly peak in Bed-2 and Bed-3 returning to pre-PEB values in Bed-4.

5. Discussion

5.1. Carbon isotopes and depositional environment

The carbon isotopes have a crucial signature excursion across the PETM that permits identification and correlation of this event globally even if it shows magnitude and shape varying from location to location from abrupt (mostly) to gradual (rare) negative shifts (Sluijs and Dickens, 2012). Here we assess this record for the GSSP outcrops based on $\delta^{13}\text{C}_{\text{carb}}$ and $\delta^{13}\text{C}_{\text{org}}$ data; for the GSSP outcrop only $\delta^{13}\text{C}_{\text{org}}$ data is available (Dupuis et al., 2003). The carbon isotope excursion (CIE) at the GSSP has three main parts: 1) a gradual decrease, 2) the CIE minimum, and 3) gradual recovery.

At Dababiya the gradual decrease in $\delta^{13}\text{C}$ is most developed in Dababiya NW, strongly condensed in the GSSP and nearly absent in the Dababiya E outcrops (Fig. 6 and 9A). This lateral variation mirrors the variable erosion/down cutting across the submarine channel

(Fig. 9B). However, at the expanded Dababiya NW record, $\delta^{13}\text{C}_{\text{carb}}$ reached minimum about 60 cm below the PEB (Fig. 6 and 9A). In the GSSP and Dababiya E outcrops the onset of minimum $\delta^{13}\text{C}_{\text{org}}$ values is also apparent but reduced to the 10 cm below the PEB. In Dababiya NW and E $\delta^{13}\text{C}_{\text{carb}}$ CIE-minimum values are reached in the middle of Bed-2 (top of zone E1) followed by gradual recovery. (No $\delta^{13}\text{C}_{\text{carb}}$ data is available for the GSSP at this interval). In contrast, $\delta^{13}\text{C}_{\text{org}}$ recovery begins much later in Bed-3 (base zone E2) in all three sections and continues to the top of the outcrops (Bed-5).

The GSSP carbon isotope trends are globally similar but differ in the gradual onset and long-term $\delta^{13}\text{C}_{\text{carb}}$ and $\delta^{13}\text{C}_{\text{org}}$ decrease in the late Paleocene (zone P5), differential duration of the minima (zone E1) and onset of recovery (early zone E2) recorded in the three Dababiya sections (Fig. 9A). Are these different signals due to local or regional conditions and/or could they reflect global conditions not generally observed in low sedimentation environments?

One explanation is that the gradual decrease in the $\delta^{13}\text{C}_{\text{org}}$ and $\delta^{13}\text{C}_{\text{carb}}$ at Dababiya NW is linked the gradual temperature increase at the end of the Paleocene (Bowen and Zachos, 2010) as a result of the North Atlantic volcanic province, Caribbean volcanic activity, and mid ocean ridge volcanism (Storey et al., 2007) all occurring during late Paleocene (Courtillot and Renne, 2003). It has also been suggested that the pre-PEB $\delta^{13}\text{C}_{\text{carb}}$ CIE-minimum reflects increased marine and atmospheric CO_2 input due to North Atlantic volcanism (Bowen and Zachos, 2010). The maximum phase of volcanic activity probably resulted in changes in ocean circulation, chemistry and heat transport (Renssen et al., 2004), which may have destabilized the methane clathrates stored in the continental shelf,

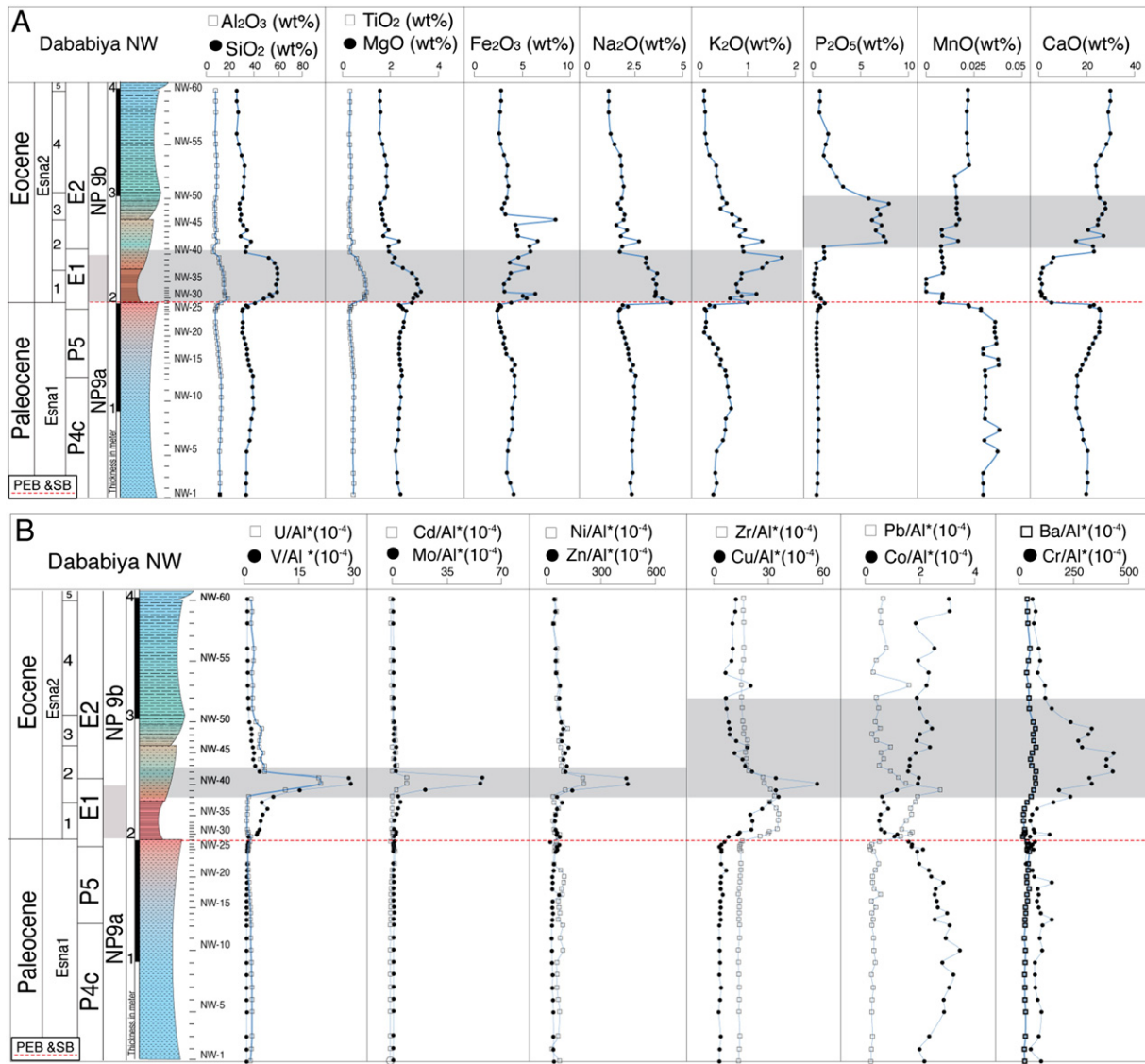


Fig. 8. A) Major elements across the Dababiya NW section. Increased Al, Si, Ti, Mg, Na and K in the lower part of PETM (50 cm above the SB) reflect high detrital input. High P and Ca present in the upper PETM suggest increased productivity. B) Al-normalized trace elements plotted against the litholog of the Dababiya NW section show abrupt increases in U, V, Cd, Mo, Ni, and Zn, which reflects increasing productivity and anoxic conditions.

releasing large quantities of methane into the water column and atmosphere. Oxidation of methane would have produced strongly ^{13}C -depleted CO_2 , which precipitated carbonates with low $\delta^{13}\text{C}$ values that could account for the $\delta^{13}\text{C}_{\text{carb}}$ CIE-minimum significantly before the $\delta^{13}\text{C}_{\text{org}}$ CIE-minimum.

In contrast, the $\delta^{13}\text{C}_{\text{org}}$ CIE-minimum is within the onset of the $\delta^{13}\text{C}_{\text{carb}}$ PETM recovery phase" (early zone E2, Bed-3) marked by increased values in the upper part of Bed-3, which is also characterized by a significant Ca-apatite increase. A possible explanation for this delayed $\delta^{13}\text{C}_{\text{org}}$ CIE-minimum is isotopically light carbon released from methane oxidation by different processes: i) increased continental silicate weathering (Kelly et al., 1996, 2005; Bowen and Zachos, 2010), ii) photosynthetic fixation of the excess atmospheric CO_2 mostly by terrestrial plants that developed during the PETM hot humid climate with formation of floodplain wetlands (Dickens et al., 1997; Bains et al., 2000; Zeebe et al., 2009), and iii) increased ocean primary productivity (Torfstein et al., 2010).

The delayed $\delta^{13}\text{C}_{\text{org}}$ CIE-minimum coincides with the maximum content of organic matter, which appears to be of terrestrial origin and thus reflects the delayed response of the continental environment to the huge light carbon input into the atmosphere. A similar delay in the

$\delta^{13}\text{C}_{\text{org}}$ CIE-minimum was observed in other PETM sections in Egypt (Khozyem et al., 2013). This delayed the $\delta^{13}\text{C}_{\text{org}}$ minimum may be limited to the onset of the recovery phase and linked with the presence of significant apatite and calcite contents (Fig. 4).

5.2. How complete is the GSSP?

5.2.1. Isotope stratigraphy

The PEB global stratotype section and point (GSSP) was placed at the base of the clay layer coincident with the steepest slope of the negative $\delta^{13}\text{C}_{\text{org}}$ CIE at Dababiya GSSP (Egypt) (Aubry and Ouda, 2003; Gradstein et al., 2004). Consequently, the base of the CIE has become the global marker for the Paleocene-Eocene boundary. In most PEB sections analyzed both $\delta^{13}\text{C}_{\text{org}}$ and $\delta^{13}\text{C}_{\text{carb}}$ values show sharp abrupt negative excursions. Similar, though less prominent, excursions are observed in $\delta^{18}\text{O}_{\text{carb}}$ and $\delta^{15}\text{N}_{\text{org}}$ profiles. Such abrupt isotopic changes likely record a hiatus at the PETM onset as observed worldwide, e.g., Egypt (Gebel Duwi, Gebel Aweina; Speijer et al., 2000, 2002; Wadi Nukhul; Khozyem et al., 2013), Italy (Forada section; Agnini et al., 2007), Spain (Zumaya section; Schmitz et al., 1998), Uzbekistan (Trabakua section; Bolle et al., 2000), DSDP Sites 401 and ODP Sites 690, 685, 689, 865, 1051, 1263,

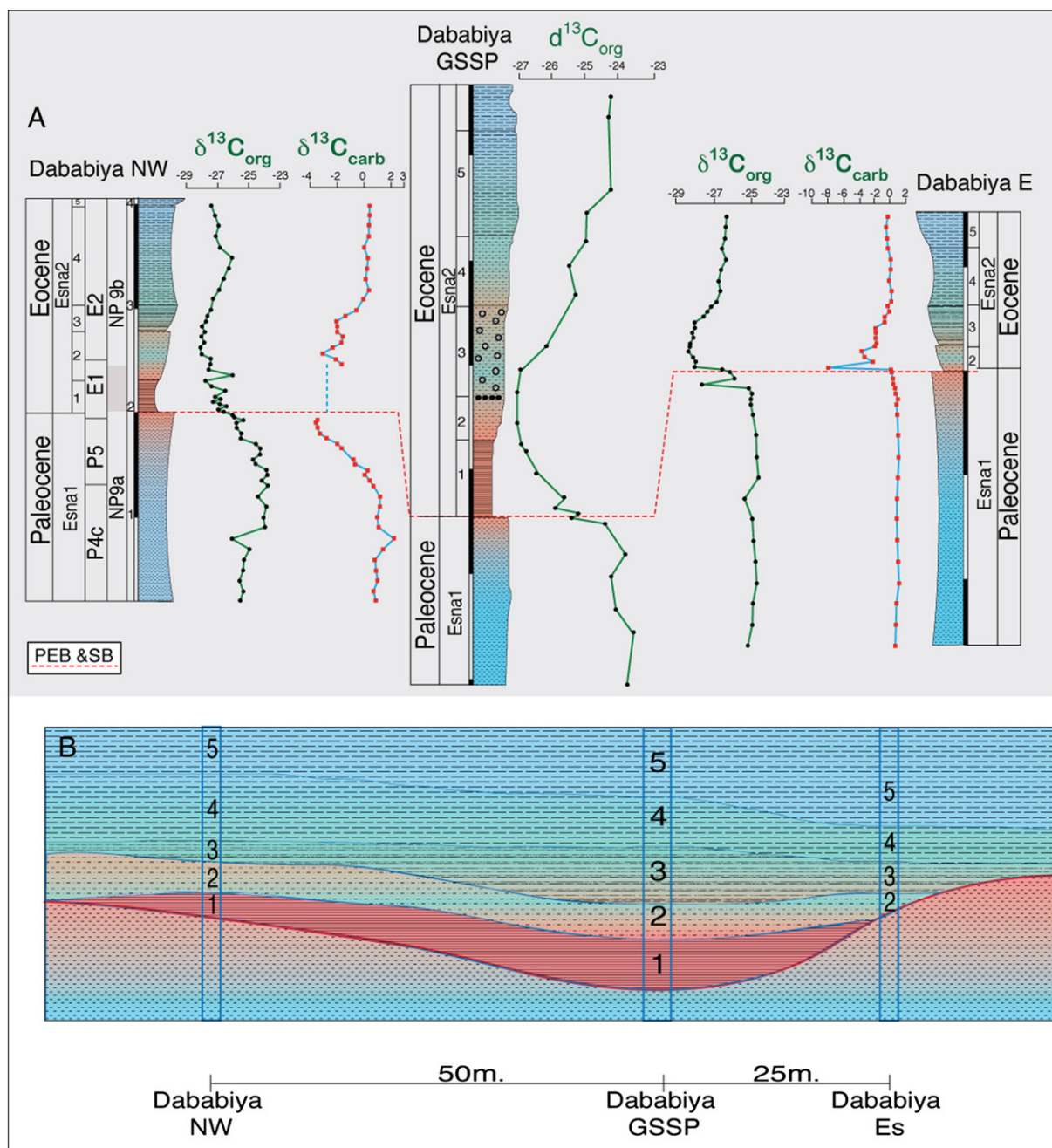


Fig. 9. A) Correlation of the three Dababiya sections (NW-GSSP-E) based on both organic Carbon isotopes, and new data obtained from inorganic carbon isotopes ($\delta^{13}\text{C}_{\text{org}}$ at Dababiya from Dupuis et al., 2003). Both $\delta^{13}\text{C}_{\text{carb}}$ and $\delta^{13}\text{C}_{\text{org}}$ in the NW section show gradual decreases beginning 60 cm below the SB and reaching the CIA-minimum for $\delta^{13}\text{C}_{\text{carb}}$ at the SB, whereas the $\delta^{13}\text{C}_{\text{org}}$ CIA-minimum is reached in the upper third of Bed 2. B) Schematic diagram showing the pinching out of Bed 1 and Bed 2 to the NW and E sides of the main GSSP, marking the deposition in an asymmetrical submarine channel.

1260B and 1172D (Katz et al., 2003; Mutterlose et al., 2007; Sluijs et al., 2008) (Fig. 10).

Evidence of a gradual decreases in the stable isotope ratios has been observed 0–2 m below the PEB, spanning an interval of about 120 ky before the PEB (Speijer et al., 2000) in marine and terrestrial sections, including Spain (Alamedilla; Lu et al., 1996), Uzbekistan (Aktumsuk; Bolle et al., 2000), Egypt (Dababiya; Aubry et al., 2007), ODP site 690 (Bains et al., 1999) and in pedogenic carbonate from Polecat Bench, Wyoming (Bowen et al., 2001).

5.2.2. Lithostratigraphy

At the Dababiya GSSP, The PEB is placed at the sequence boundary (SB) that marks a change in lithology from marine hemipelagic to

coarser sediments linked to increased fluvial discharge from shallower environments (Schulte et al., 2011). Sediments are characterized by increased detrital components (e.g., quartz, phyllosilicates, feldspars) and an abrupt decrease in carbonate contents (Fig. 4A). The decreased CaCO_3 contents could be due to carbonate dissolution and/or dilution due to increased detrital input (Bolle et al., 2000; Khozyem et al., 2013). Because of the location of the GSSP in a submarine channel, there is significant lateral variation (Schulte et al., 2011; Khozyem et al., 2014; this study). Bed-1 is most expanded at the GSSP outcrop (deepest part of channel), decreases to about half at 50 m to the northwest (NW section) and is absent 25 m to the east (E section, Fig. 9).

The change in the whole rock compositions in the NW and E sections further supports this observation (Fig. 4). The NW section shows an

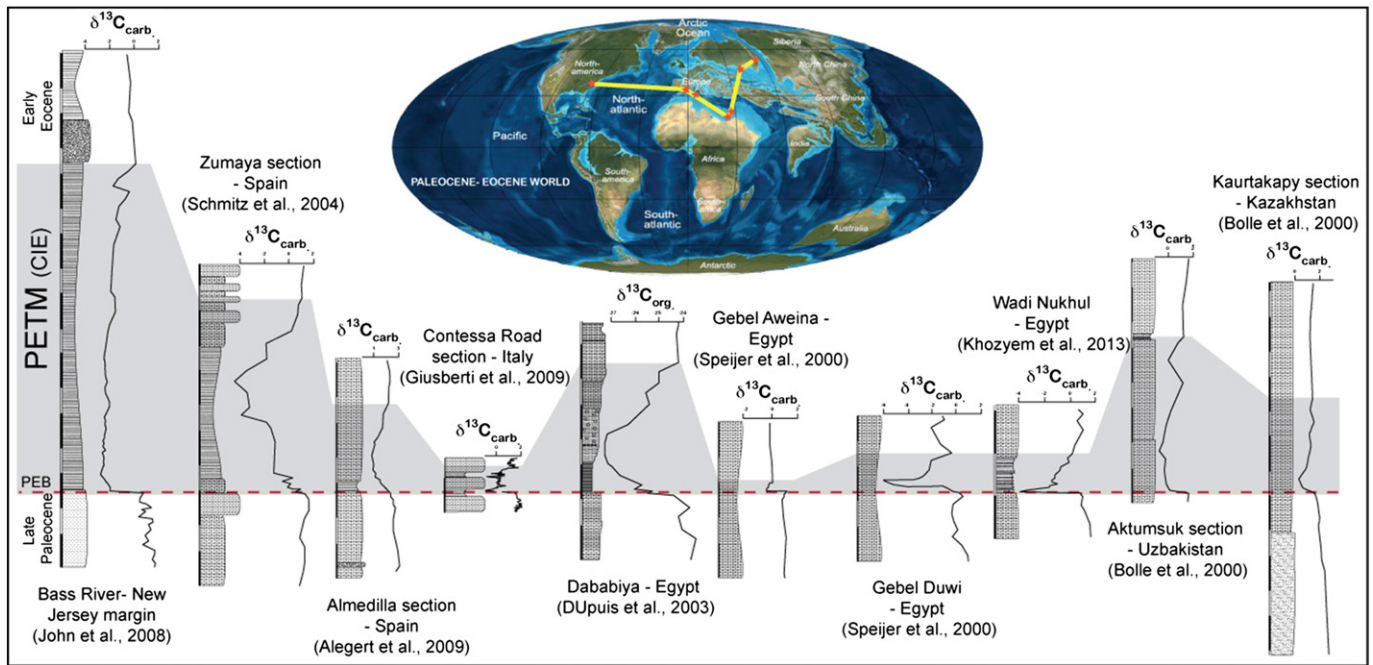


Fig. 10. Local and global correlation of the PETM interval with the Dababiya GSSP section based on correlation of the organic and inorganic carbon isotope shifts (modified after Khozyem et al., 2013).

abrupt change that persists for 58 cm above the PEB and SB with increased phyllosilicate, quartz, and feldspar but no change in Ca-apatite. At the E section the whole rock composition changes sharply at the PEB, with notable increases in quartz, feldspar, and phyllosilicate and an abrupt decrease in calcite about 5 cm above the SB. These abrupt whole rock changes in the E section are likely linked to erosion, weathering and paleotopography. Based on field observation, lithostratigraphy and whole rock mineralogy deposition of the Dababiya GSSP occurred along channel banks (Dupuis et al., 2003; Schulte et al., 2011; Khozyem et al., 2014) and more particularly an asymmetric submarine channel that extended 25 m eastward and about 150 m north-west with maximum width of about 200 m and maximum depth of about 0.88 m.

So how complete is the Dababiya GSSP? The facts are that the GSSP was chosen in a submarine channel with the Paleocene-Eocene boundary marked by a sequence boundary and erosional surface, where major lateral variations in sediment deposition/erosion are observed within and outside the channel. The GSSP therefore does not represent a complete sedimentary record across the PE boundary. Moreover, the sequence boundary and erosion can be traced over hundreds of kilometers through Egypt and even worldwide. Consequently, the PE transition is often incomplete worldwide with a hiatus spanning the latest Paleocene and earliest Eocene and in many cases missing the recovery part (i.e. New Jersey shelf sections) that may be due to the superposition of a rapid (albeit small-scale) sea-level rise and massive influx of terrestrial material. We conclude that the GSSP represents an incomplete but locally expanded PETM sequence that is useful for evaluating the global records, which are generally less complete and contain more major hiatuses.

5.3. Mineralogical proxies: paleoenvironmental implications

5.3.1. Bulk rock proxies

Whole rock and clay minerals and their ratios, such as Detrital index (calcite/detritus ratio used to show depletion in calcite), kaolinite/smectite, and kaolinite/illite + chlorite are good proxies to track paleoclimatic changes (Chamley, 1989; Adate et al., 2002). The abrupt

change in whole rock composition that characterizes the PEB is linked to phyllosilicate, quartz and feldspar enrichments to the detriment of calcite and represents high detrital input as also noted by decreasing calcite/detritus ratios (Fig. 4A). At the PEB, the increased detrital input negatively affects the calcite content resulting in minimum values that could be due to leaching of the carbonate contents under acid conditions and/or dilution by increased detrital input. Dababiya data show these changes in the whole rock composition at the PEB and SB due to high terrigenous input associated with increased erosion and transport of detrital material in response to climatic and sea level changes (Khozyem et al., 2013). Schulte et al. (2011) interpreted the increased detrital input and the abrupt higher phyllosilicate content a result of increased riverine input during a period of low or rising sea level. Speijer and Wagner (2002) explained the increased detrital input as reworking linked to the transgressive system tract (TST) during a period of high silicate weathering. Based on these interpretations and the paleotopography of the depositional basins, we interpret the PETM low calcite/high detrital interval at Dababiya GSSP as increased fluvial discharge into a submarine channel during a TST period.

The increase in Ca-apatite coincides with a gradual increase in calcite (Fig. 4A), which can be interpreted as increased surface productivity and onset of recovery (Torfstein et al., 2010). The Ca-apatite enrichment can also be explained by remobilization of phosphate from detrital material and/or released from decaying organic matter that reflects the termination of anoxic conditions.

5.4. Clay mineral proxies

The diagenetic overprint on clay minerals generally occurs at burial depths exceeding 2 km (Chamley, 1998). Sediments from Dababiya NW show no sign of burial diagenesis, as indicated by the variable presence of smectite and low content of mixed layer illite-smectite (e.g., Bolle et al., 2000). Detrital input is responsible for the clay mineral distribution in marine sediments (Millot, 1970). The clay rich interval (samples NW28-NW40, Fig. 4A and 5) consists of a lower part enriched in smectite and no change in the kaolinite/smectite ratio from the PEB-SB to the top of Bed-1, and an upper part with low smectite, relatively

high kaolinite/smectite ratio and higher kaolinite, chlorite, illite-smectite and palygorskite contents. This reflects low to medium detrital input under semi-arid conditions during the lower part, and increased detrital input during the upper part as evident by increased quartz contents, reflecting increased runoff.

Chlorite and mica predominate in continental areas marked by steep relief where active mechanical erosion restrains soil formation, particularly during periods of enhanced tectonic activity, or in cold and/or desert regions where low temperatures and low rainfall reduce chemical weathering (Millot, 1970; Chamley, 1998). This suggests a scenario of a tectonically stable southern Tethys during the Paleocene-Eocene interval with low chemical weathering (Bolle and Adatte, 2001; Khozyem et al., 2013) and erosion of illite, chlorite, and illite-smectite transported into the depositional basin by seasonal riverine input (Fig. 4A and 5).

High kaolinite content is generally interpreted as an indicator of tropical weathering (Srodon, 1999). In Dababiya NW the kaolinite content is low, except in the middle of Bed-2, the top of the weathered interval. The higher kaolinite in this interval is most likely of detrital origin

since clay minerals shows the same variations as chlorite, palygorskite and IS.

The mineralogy of the two horizons is marked by increased detrital input and reflects the nature of weathering processes that initiated at the sequence boundary. Intensive physical weathering began under semi-arid conditions associated with occasional but extreme rainfall that triggered transport of eroded material into the submarine channel. Higher up in the section sediments indicate a climate gradually changing to seasonal and/or arid conditions as indicated by the gradual return of phyllosilicates to values observed below the PEB-SB.

5.5. Proxies from element associations and element ratios

Cluster analysis (using Minitab 11 software) performed on major and trace element concentrations identified three main groups with characteristic enrichment/depletion that reflect successive climatic and environmental changes during the PETM. The three groups represent: (a) detrital input and weathering indexes, (b) redox conditions and (c) productivity sensitive trace elements. The interpretation of

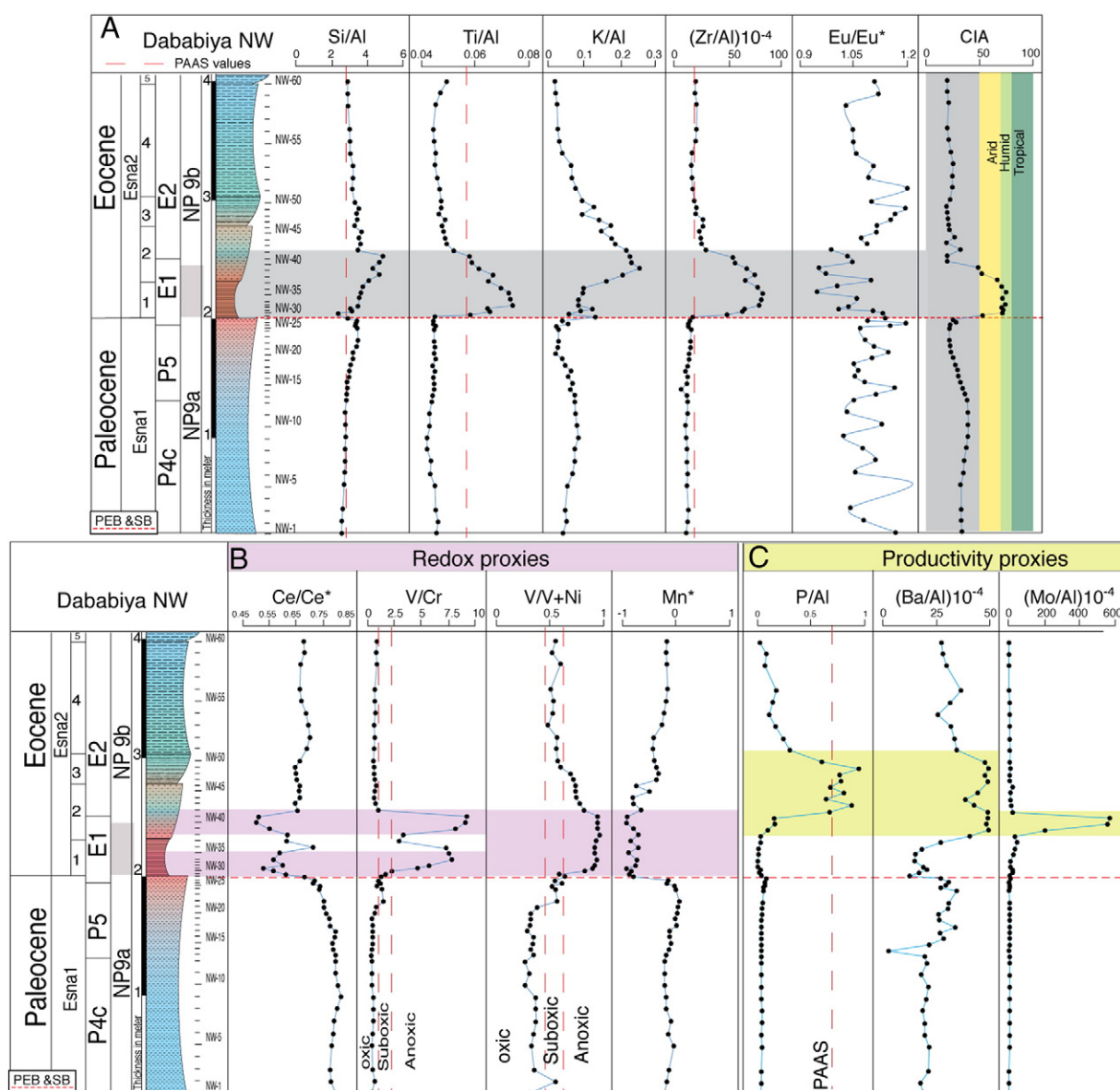


Fig. 11. A) Detrital input proxies, Eu-anomaly and Chemical index of alteration (CIA). Increased Si, Ti, K, Zr and weathering indexes are associated with a negative Eu/Eu* ratio. B) Ce/Ce* and redox parameters (V/Cr, V/V + Ni, and Mn*) show the different anoxic intervals recorded at the Dababiya NW section. C) Plot of paleoproductivity parameters (P, Ba and Mo).

these geochemical groups was further supported by the stratigraphic variations of element ratios commonly used as proxies for redox conditions, detrital input, weathering rates and productivity (e.g., Eu anomaly ($\text{Eu}/\text{Eu}^* = (3\text{Eu}_n/[2\text{Sm}_n + \text{Tb}_n])$, Zhang et al., 2008), Ce anomaly ($\text{Ce}/\text{Ce}^* = (\text{Ce}_n/[(\text{La}_n + \text{Pr}_n)/2])$), chemical index of alteration ($\text{CIA} = [\text{Al}_2\text{O}_3]/[\text{Al}_2\text{O}_3 + \text{CaO}^* + \text{K}_2\text{O} + \text{Na}_2\text{O}] \times 100$, where CaO^* represents the calcium in the silicate fraction only, and moles are used rather than weight % to emphasize mineralogical changes, Nesbitt and Young, 1984, 1989; Price and Velbel, 2003), $\text{Mn}^* = \log[(\text{Mn}_{\text{sample}}/\text{Mn}_{\text{PAAS}})/(\text{Fe}_{\text{sample}}/\text{Fe}_{\text{PAAS}})]$, V/Cr , and $\text{V}/(\text{V} + \text{Ni})$, P/Al , Ba/Al , Cd/Al , Mo/Al as well as TOC contents (Cullers, 2002; Brumsack, 2006; Riquier et al., 2006; Tribouillard et al., 2006; Kraal et al., 2010).

5.6. Detrital input

As observed from the distribution of bulk and clay minerals at Dababiya NW, the increased detritus fraction (quartz + phyllosilicate + feldspar) is affected positively by the abundance of chemical elements linked to detrital input (Fig. 4A). The first group of elements indicates the detrital input and weathering rate, including Si/Al , Ti/Al , K/Al , Zr/Al , Eu/Eu^* , and CIA, that show abrupt changes between the sequence boundary to the middle part of Bed 2 (Fig. 11A). Below the SB the recorded mean values of the detrital indicators are Si/Al (3.1), Ti/Al (0.04), K/Al (0.3), Zr/Al [$13(10^{-4})$], Eu/Eu^* (1.2) and CIA (30.86). At the SB, a persistent change from sample 28 to 42 records mean values of 3.7, 0.06, 0.4, $28(10^{-4})$, 7.3, 1.1, and 56.92, respectively, corresponding to the high phyllosilicate interval; all Al-normalized elements and their ratios are enriched comparable to the PAAS (Fig. 11A). Above sample NW42 all Al-normalized elements and the ratios used as detrital input indicator return to the mean values observed below the SB.

The Al-normalized Si, Ti, K, and Zr contents, combined with the Eu/Eu^* ratios can be used to distinguish detrital material from different sources with a riverine origin as the most recognizable source (Bertrand et al., 1996; Murphy et al., 2000; Pujol et al., 2006; Khozyem et al., 2013). The enriched clay interval of Dababiya NWs reflects a strong period of fluvial discharge, which was the main source of weathered material into the ocean (e.g., Schulte et al., 2011), as indicated by high Ti/Al , and Zr/Al ratios. The source of the detritus in the NW section appears to be homogenous as indicated by the uniform stratigraphic distribution of both Si/Al and K/Al ratios (Riquier et al., 2006).

5.7. Redox conditions and productivity

The second cluster of elements includes redox sensitive elements and ratios (Fig. 11B). The Ce/Ce^* ratio shows a notable decrease from the mean 0.78 to 0.49 at the SB. Low Ce/Ce^* ratios were found at the base of Bed 1 (base zone E1) and the middle part of Bed 2 (top of zone E1; Fig. 11B). These negative Ce/Ce^* ratios are associated with sharp peaks in V/Cr ratios and indicate anoxic conditions (Riquier et al., 2006). Above the PEB (zone E1 to base E2) the $\text{V}/(\text{V} + \text{Ni})$ ratio sharply increases with minimum Mn^* values at 10 cm above the PEB.

Removal of dissolved major, trace and rare earth elements from the water column and their incorporation in sediments depends on biotic and abiotic processes and redox conditions in the water column and the water-sediment interface (e.g., Tribouillard et al., 2006). In oxic environments trace elements are scavenged by precipitating Fe-Mn oxyhydroxides, whereas in dysoxic and anoxic environments, trace element enrichments are linked to redox cycles in the sediment-water interface and associated microbial activities (Lyons et al., 2003; Sageman and Lyons, 2003; Algeo and Maynard, 2004; Riquier et al., 2006; Tribouillard et al., 2006). Therefore the MEs and TEs can provide insights into the paleo-depositional environments at the PETM.

Changes in bottom water conditions can be interpreted based on different element ratios (e.g., V/Sc , V/Cr , Ni/Co , U/Th , $\text{V}/\text{V} + \text{Ni}$ etc.) and Al-normalized contents of redox sensitive and chalcophile elements

(e.g., Fe, Mn, U, V, Zn, Pb, Cu, Ni) (Joachimski et al., 2001; Algeo and Maynard, 2004; Cruse and Lyons, 2004; Rimmer, 2004; Pujol et al., 2006). However, some of these elements are typically associated with hydrothermal activity (e.g., Pb, Zn, Cu, Co, Ag, Mo) and the cause of their enrichment remains often ambiguous (Cruse and Lyons, 2004).

The Ce-anomaly is one of the strongest indicators for water column oxygenation. Seawater contains low concentration of Ce because it can be easily oxidized to the 4^+ insoluble state under oxic conditions (Holser, 1997; Shields and Stille, 2001). However, the Ce^{4+} tend to be lost from the sediments under reducing conditions. A similar process leads to Mn enrichment in sediments deposited under oxic condition. Mn^* (Cullers, 2002) is the best expression of the Mn concentrations linked to redox conditions, where Mn^{2+} replaces Ca in Ca-rich sediments during the diagenetic processes and forms Mn-bearing carbonate. Vanadium is strongly coupled with the redox cycle of both Mn and Fe-oxyhydroxides and could be incorporated into Mn-Fe bearing minerals (Tribouillard et al., 2006). Another source of V is the sedimentary biomass from nitrogen fixing bacteria (Anbar, 2004; Grosjean et al., 2004). Low Mn contents can be indicative of dysoxic bottom water conditions given that under reducing conditions at the sediment/water interface, soluble Mn^{2+} diffuses from the sediments into the oxygen-depleted bottom waters (Landing and Bruland, 1980, 1987; Bruland, 1983).

5.7.1. Dababiya paleoenvironment

This area was part of the southern Tethys margin, which was tectonically stable during the late Paleocene to early Eocene. In this environment, Al-normalized contents of chalcophile elements (Algeo and Maynard, 2004; Pujol et al., 2006) and their ratios can also be used to constrain the water column oxygenation during deposition of the PETM sediments.

Schulte et al. (2011, 2013) inferred the presence of one anoxic interval at the Dababiya GSSP. In this study the Ce/Ce^* data combined with other redox proxies marks one additional anoxic interval (Fig. 11B). The two Ce/Ce^* negative shifts in the lower part of the PETM interval at NWs mark each anoxia with their own characteristics.

The lower anoxic level is characterized by the negative Ce/Ce^* shift with a positive excursions in V/Cr , and $\text{V}/\text{V} + \text{Ni}$ values, a decrease in Mn^* , no change in the Al-normalized trace elements V/Al , U/Al , Zn/Al , Cu/Al , and Ni/Al (Fig. 8 and 11B) and the presence of disseminated idiomorphic pyrite crystals. These features observed in the lower anoxic interval may be linked to exhalation of oxygen from the ocean due to an acidifying ocean. Another reason for these lower anoxic conditions could be the high detrital input linked to the rapid sea level rise during the PETM due to thermal expansion of the seawater (Schulte et al., 2013). In addition, the released CO_2 from the ocean due to clathrate melting acts as atmospheric greenhouse gases. The environmental response is the drawdown of excess CO_2 by silicate weathering on land and transport to the ocean by streams particularly during the early stage of the PETM associated with the TST. Other oxygen-forcing processes may act, such as temperature/salinity-driven water column stratification and/or methane oxidation (Dickson et al., 2014). Mixing of fresh water loaded with suspended nutrients result in water column stratification, and/or development of eutrophic conditions due to the low light penetration as noted by the presence of important bacterial activity, mainly from sulphur reducing and nitrogen-fixing bacteria (Fig. 12 and 13).

The upper anoxia level is characterized by the negative Ce/Ce^* shift coincident with increased V/Cr and a continuous increase in $\text{V}/\text{V} + \text{Ni}$ and depletion in Mn^* (Fig. 8 and 11B). These changes coincide with an abrupt increase in V/Al , U/Al , Zn/Al , Cu/Al , Ni/Al , common pyrite framboids and EPS-like of sulfur reducing bacteria (Fig. 12 and 13) the presence of N-fixing bacteria indicated by steady negative $\delta^{15}\text{N}$ values (Fig. 12). Thus the characteristics of each negative Ce/Ce^* anomaly reflects the variable nature of anoxia, including increased surface water

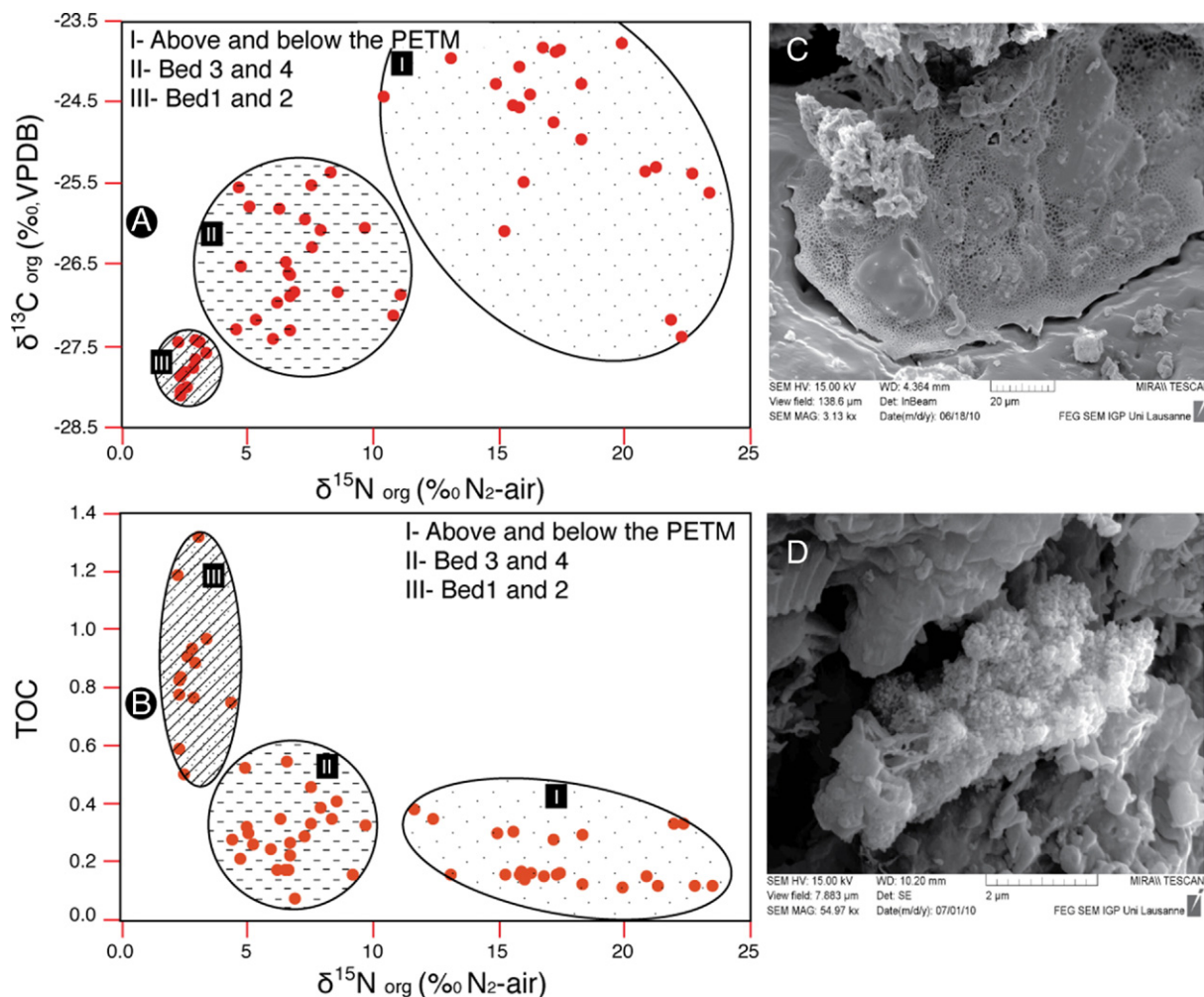


Fig. 12. A) Cross plot of $\delta^{13}\text{C}_{\text{org}}$ vs. $\delta^{15}\text{N}_{\text{org}}$; B) TOC vs. $\delta^{15}\text{N}_{\text{org}}$ shows differences in organic matter types above and below the PETM and at the interval marked by increased weathering. C) SEM micrographs shows EPS-like structure of Cyanobacteria. D) SEM micrograph shows EPS-like structure of sulfur reducing bacteria.

productivity and accumulation of organic matter debris at the time of the upper anoxia.

5.7.2. Anoxia linked to ocean acidification

Anoxia appears to be linked to ocean acidification with the formation of anhydrite (Fig. 13). Whiticar (1999) discussed the relationship between sulphate reduction and methane release (Fig. 13A), he concluded that the release of methane produces free SO^{+4} that easily reduce to HS^- under acidic-anaerobic conditions (HCO_3^-) at the anaerobic/aerobic interface where sulphides oxidize in the presence of NO as oxidizing agent (Campbell et al., 1992; Whiticar, 1999; Jenkyns, 2010). Based on these processes, we suggest that the lower anoxic interval resulted in precipitation of disseminated euhedral pyrite crystals in sediments (Fig. 13B, photos 1, 2). The upper anoxic level is associated with the accumulation of organic matter (Fig. 13B; photo 3 and 4), the oxidation of framboidal pyrite ($<5 \mu\text{m}$, Fig. 13B; photos 5 and 6) formed by bacterial activity under anoxic water column conditions (Wilkin et al., 1996, 1997; Wignall et al., 2005; Riquier et al., 2006). This is followed or accompanied by concomitant precipitation of primary anhydrite in a medium saturated with dissolved CaCO_3 (Fig. 13B; photos 10 and 11).

The third element association includes phosphorous (P_{tot}) and productivity sensitive trace elements (Mo, Cd, Ba, and P), which show high concentrations at Dababiya NW in the second anoxic interval (top zone E1, middle Bed-2), generally associated with high TOC (Fig. 11C) and Ca-apatite contents. Ba and P_{tot} show a sharp increase in the middle of Bed 2 (sample NW-40), which persists up to the top of the PETM

interval. High nutrient content at the base of this interval is suggested by increased trace element concentrations (Mo, Cd, Ni, Zn and Cu) associated with the second Ce/Ce* negative peak.

5.8. Nitrogen isotope variations: shallow sea eutrophication

Nitrogen is a main nutrient in the ocean and its stable isotope ratio is a promising proxy for delineating eutrophication of oceans during the PETM. Nitrogen isotope fractionation of sedimentary organic matter helps trace the biological cycle of nitrogen in the marine environment, including the process of nitrogen fixation, mineralization, nitrification, heterotrophic denitrification and anaerobic ammonia oxidation (Beaumont and Robert, 1999; Spangenberg et al., 2013). This provides important clues to the trophication level in the aquatic ecosystem. The marine N cycle during the PETM was similar to today. In the modern ocean, N_2 fixation is mainly associated with areas of low productivity and low accumulation of sedimentary organic carbon (Kuypers et al., 2004). The conversion of nutrient N to N_2 predominantly occurs in the oxygen-depleted waters and sediments underlying upwelling zones characterized by high productivity and high rates of organic carbon accumulation. The nitrogen depletion is a phenomenon linked to the high ocean surface production and intense oxygen minima as observed in the present day ocean (Ohkouchi et al., 1997, 2006; Farrimond et al., 2004; Kuypers et al., 2004; Dumitrescu and Brassell, 2006; Jenkyns, 2010).

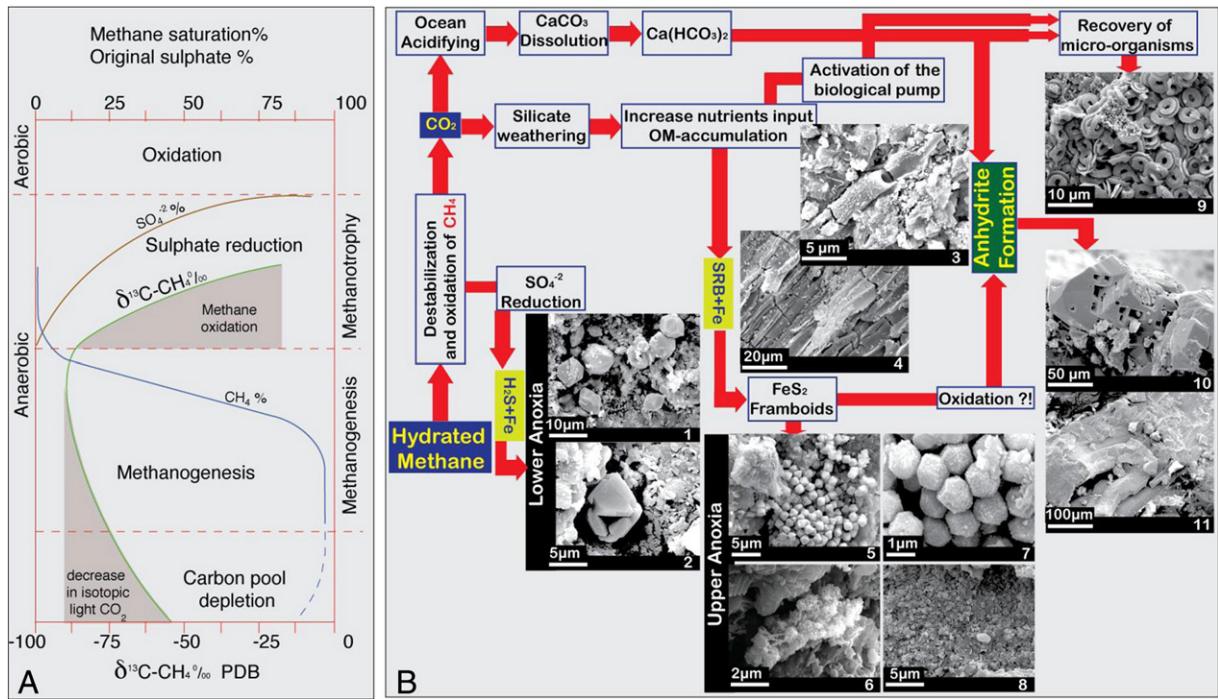


Fig. 13. A) Illustration of different processes implicated in methane hydrate release from the continental shelf (after Whiticar, 1999). B) Schematic diagram illustrating the mechanisms leading to two anoxic levels observed at the NW section and the deposition of anhydrite. SEM micrographs 1 and 2 show individual pyrite crystals formed at the sediment/water interface within the lower anoxic interval; SEMs 3 and 4 show different fragments of terrestrial plants; SEMs 5, 6 and 7 illustrate pyrite framboids found in the upper anoxic interval; SEM 8 shows an oxidized framboid grain in the cavity of anhydrite; SEM 9 illustrates nanofossils accumulated during the recovery phase, and SEMs 10 and 11 illustrate anhydrite layers observed within the recovery interval.

The nitrogen isotopes composition of kerogens covers a broad range of almost 23‰ indicating the compositional variability of organic matter where values $>7\text{‰}$ indicate marine to open marine organic matter and values $<7\text{‰}$ reflect terrestrial and mixed organic matter contents (Peters et al., 1978). The relatively low $\delta^{15}\text{N}$ values, close to that of the modern atmospheric N_2 ($\delta^{15}\text{N} \approx 0\text{‰}$), may result from primary contribution of microbial N_2 fixers as oxygenic photosynthetic cyanobacteria and/or input of nitrogen-fixing terrestrial plant debris into the marine sediments (e.g., Fio et al., 2010).

The cross plot $\delta^{15}\text{N}$ - $\delta^{13}\text{C}_{\text{org}}$ helps unravel the nature of the sedimentary organic matter and depositional conditions at Dababiya NW (Fig. 7 and 12). Samples can be grouped into three distinctive fields: I) open marine organic matter supply ($> +10\text{‰}$ $\delta^{15}\text{N}_{\text{org}}$ and -27.5 to -23.5‰ $\delta^{13}\text{C}_{\text{org}}$) for the group of samples representing the late Paleocene and above the PETM level; II) mixed organic sources ($\approx +4$ to $+10\text{‰}$ $\delta^{15}\text{N}_{\text{org}}$ and -27.5‰ to -25.2‰ $\delta^{13}\text{C}_{\text{org}}$) of the PETM excluding the enriched clay interval and anoxic levels; and (III) bacterial derived organic matter ($<3\text{‰}$ $\delta^{15}\text{N}$ and -27.5 to -28.5‰ $\delta^{13}\text{C}_{\text{org}}$) characterizing the interval including anoxia levels (Fig. 12; photo C and D).

As noted in the middle part of Bed-2 at Dababiya NW, the $\delta^{15}\text{N}$ reached minimum values at the same time as maximum TOC concentrations (Fig. 12B). This suggests mainly a cyanobacterial contribution, probably due to the introduction of soil microbial biomass from river waters into the shallow-shelf system (e.g., Fio et al., 2010). Cyanobacteria are known to be capable of surviving in high-stress environments (e.g., Roszak and Colwell, 1987; Ben-Jacob et al., 2000; Cao et al., 2009) and also may be responsible for increasing oxygen content in the water column and nitrification. This could be associated with bacterial activities (sulphur reducing bacteria and N-fixers) near the onset of the PETM recovery phase. Similarly, the N_2 fixation was the source of nutrient N in vast areas of the Mesozoic oceans characterized by strong oxygen depletion, high nutrient N loss, and high rates of organic carbon accumulation under anoxic conditions (Meyers et al., 2006; Knies et al., 2008).

5.9. The PETM scenario

The late Paleocene to early Eocene transition experienced a series of changes related to the progressive warming potentially linked with the northeastern Atlantic volcanic activity (Courtillot and Renne, 2003) and changes in ocean circulation (Bice and Marotzke, 2002). New geochemical and mineralogical data from the Dababiya GSSP sheds new light on current global PETM scenarios particularly with respect to low latitude continental shelf environments. Four major phases of the PETM can be identified (Fig. 14).

5.9.1. Phase 1

Volcanism during the late Paleocene in the North Atlantic volcanic province, Caribbean and mid-ocean ridge areas (Courtillot and Renne, 2003; Storey et al., 2007) led to gradual increase in ocean temperatures and changes in ocean circulation (Dickens et al., 1995, 1997), which affected methane hydrates stored on the continental shelf (Fig. 14). The gradual decrease in $\delta^{13}\text{C}_{\text{org}}$ and $\delta^{13}\text{C}_{\text{carb}}$ preceding the sequence boundary at Dababiya GSSP and also observed at Alamedilla, Spain (Lu et al., 1996), reflects this changing environment.

5.9.2. Phase 2

During the second phase submarine volcanism resulted in ocean warming of about 5°C leading to thermal expansion and a sea level rise of about 5 m, which destabilized methane clathrates (Speijer and Wagner, 2002; Sluijs et al., 2008) (Fig. 14). The release and oxidation of this methane gas consumed sea water oxygen and led to the first anoxia observed at the base of the PETM interval (zone E1) accompanied by ocean acidification inducing the shoaling of the CCD (Zachos et al., 2008). Phase 2 is represented at Dababiya NW by the clay-rich lower anoxic interval marked by a negative Ce-anomaly, abrupt increase in V/Cr and V/V + Ni ratios and negative Mn^* with no change in other redox proxies.

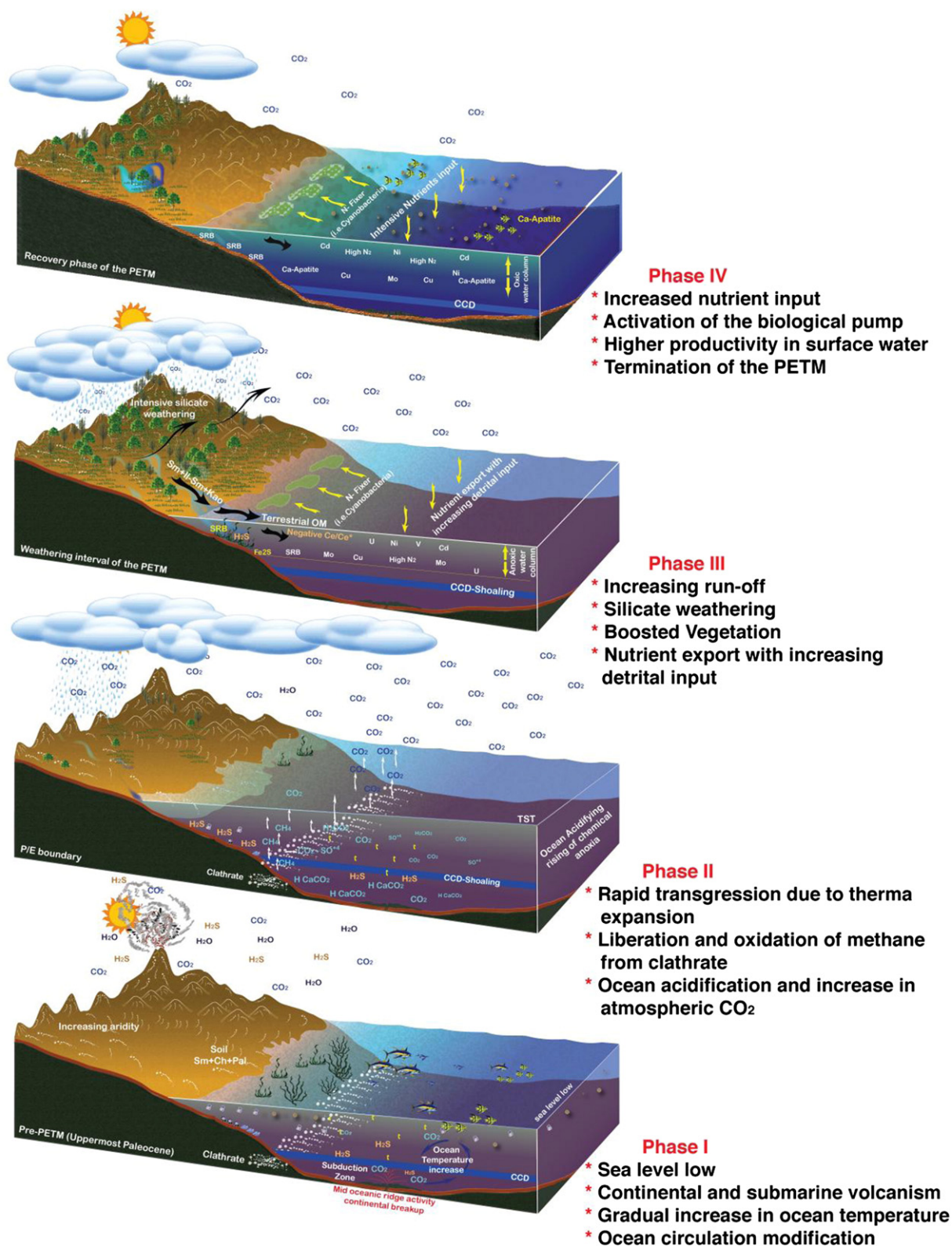


Fig. 14. Block diagrams representing the four phases of the PETM event: Phase 1 – gradual warming during late Paleocene, Phase 2 – PEB interval, Phase 3 – intensive silicate weathering phase, and phase 4 – marine recovery and drawdown of atmospheric CO₂. Note that this scenario is partly based on [Bowen and Zachos \(2010\)](#) with integrated results obtained from this study.

5.9.3. Phase 3

During the subsequent phase 3 methane gas oxidized to CO₂ at the water/atmosphere interface, thus contributing to greenhouse gases ([Fig. 14](#)). The additional CO₂ resulted in hot humid climate conditions

globally with a high precipitation. These conditions have been identified by increased kaolinite inputs and stable oxygen isotope ratios ([Bolle et al., 2000, 2001](#)). The resulting weathered terrestrial materials were carried to the oceans by streams and fluvial discharges ([Schulte et al.,](#)

2011) accompanied by terrestrial organic matter. The organic matter led to development of anoxic conditions fostering bacterial activity (SRB and Cyanobacteria) and gradually increasing oxygen by fixation of nutrients. Biosphere feedback during the PETM is thus a direct response to extremely high tropical temperatures (Huber, 2008), seasonal aridity in continental interiors (Wing et al., 2003), and the release of substantial quantities of CO₂ to the ocean/atmosphere system.

5.9.4. Phase 4

Environmental recovery marks the last phase of the PETM (Fig. 14). At this time, nutrients flux from land to the ocean was driven by intensive continental weathering, which associated with ocean surface productivity, activated the biological bump, thus decreasing ocean acidity. The recovery phase is marked by a gradual increase in carbon isotopes values and abundance of phosphorous with fixation of Ba as a result of more oxic conditions.

6. Conclusions

- (1) The Dababiya GSSP is located in the deepest part of an asymmetric 200 m wide submarine channel with the Paleocene-Eocene boundary (PEB) marked by a sequence boundary (SB) and variable erosion surface. The same SB and major hiatus can be traced over hundreds of km through Egypt as well as worldwide. The Dababiya GSSP therefore does not represent a continuous sedimentation record but has a more expanded PETM record than most PEB sections worldwide and hence is invaluable for global correlations and reconstruction of the PETM events.
- (2) $\delta^{13}\text{C}_{\text{carb}}$ and $\delta^{13}\text{C}_{\text{org}}$ profiles show a gradual decrease during the latest Paleocene (zone P5) with the CIE-minimum just above the SB. This early PETM onset can be linked to intensified North Atlantic volcanism.
- (3) The CIE-minimum in $\delta^{13}\text{C}_{\text{carb}}$ coincides with the SB and PEB, whereas the recovery begins in the middle of Bed-2 and E1/E2 zone boundary. The $\delta^{13}\text{C}_{\text{org}}$ CIE-minimum is delayed coinciding with the onset of $\delta^{13}\text{C}_{\text{carb}}$ recovery, whereas the $\delta^{13}\text{C}_{\text{org}}$ recovery begins in the lower part of Bed-3 (lower zone E2). The delayed $\delta^{13}\text{C}_{\text{org}}$ recovery may reflect carbon cycle effects (e.g. continental silicate weathering, increased rate of organic carbon burial, and increased ocean productivity). Return to normal background values occurred in the middle to upper zone E2 (Beds-3 and 4).
- (4) Strong dissolution (ocean acidification) and anoxia is indicated by the Ce-anomaly clay-rich interval above the PEB (lower zone E1, Bed-1), which may be linked to chemical anoxia related to methane release and oxygen exhalation from seawater. A second Ce-anomaly and anoxic event (upper zone E1, lower Bed-2) corresponds to an abrupt change in all redox parameters (V, U, Mo, Cd, etc.) and is associated with the maximum accumulation of organic matter. Recovery follows the second anoxic event and is marked by increased P and Ba indicating restoration of oxic conditions and ocean re-nitrification.

Acknowledgements

We thank the reviewers for their helpful comments, critique and suggestions for improvements of this MS. We are grateful to T. Monnier, J. C. Lavanchy and P. Vonlanthen for their assistance during analyses of total phosphorus, XRF and SEM determinations. Karl Föllmi's comments and advice on an earlier draft are very much appreciated. We are grateful to the Egyptian Ministry of state for Environmental Affairs and the President of the International Committee of Stratigraphy for providing the necessary permits for this studies as well as we grateful to the University of Lausanne for their financial support.

Appendix A. Supplementary data

Supplementary data to this article can be found online at <http://dx.doi.org/10.1016/j.palaeo.2015.04.003>.

References

- Adatte, T., Stinnesbeck, W., Keller, G., 1996. Lithostratigraphic and mineralogic correlations near K/T boundary clastic sediments in northern Mexico: Implication for origin and nature of deposition. *Geol. Soc. Am. Spec. Pap.* 307, 211–226.
- Adatte, T., Keller, G., Stinnesbeck, W., 2002. Late Cretaceous to early Paleocene climate and sea-level fluctuations: the Tunisian record. *Paleogeogr. Paleoclimatol. Paleocool.* 178 (3–4), 165–196. [http://dx.doi.org/10.1016/S0031-0182\(01\)00395-9](http://dx.doi.org/10.1016/S0031-0182(01)00395-9).
- Agnini, C., Fornaciari, E., Rio, D., Tateo, F., Backman, J., Giuseberti, L., 2007. Responses of calcareous nannofossil assemblages, mineralogy and geochemistry to the environmental perturbations across the Paleocene/Eocene boundary in the Venetian Pre-Alps. *Mar. Micropaleontol.* 63, 19–38.
- Alegret, L., Ortiz, S., 2006. Global extinction event in benthic foraminifera across the Paleocene/Eocene boundary at the Dababiya Stratotype section. *Micropaleontology* 52 (5), 48–63.
- Alegret, L., Ortiz, S., Arenillas, I., Molina, E., 2005. Paleoenvironmental turnover across the Paleocene/Eocene Boundary at the Stratotype section in Dababiya (Egypt) based on benthic foraminifera. *Terra Nova* 17, 526–536.
- Alegret, L., Ortiz, S., Molina, E., 2009. Extinction and recovery of benthic foraminifera across the Paleocene–Eocene Thermal Maximum at the Alamedilla section (Southern Spain). *Palaeogeogr. Palaeoclimatol. Palaeocool.* 279, 186–200.
- Algeo, T.J., Maynard, J.B., 2004. Trace-element behavior and redox facies in core shales of Upper Pennsylvanian Kansas-type cyclothems. *Chem. Geol.* 206, 289–318.
- Anbar, A.D., 2004. Molybdenum stable isotopes: observations interpretations and directions. *Rev. Mineral. Geochem.* 55, 429–454.
- Aubry, M.-P., Ouda, K., 2003. Introduction. In: Ouda, K., Aubry, M.-P. (Eds.), *The Upper Paleocene – Early of the Upper Nile Valley, Part 1, Stratigraphy*. Micropaleontology Press, New York, pp. ii–iv.
- Aubry, M.-P., Berggren, W.A., Cramer, B., Dupuis, C., Kent, D.V., Ouda, K., Schmitz, B., Steurbaut, E., 1999. Paleocene/Eocene boundary sections in Egypt. In: Ouda, K. (Ed.), *Late Paleocene–Early Eocene Events from North Africa to the Middle East, Symposium. First International Conference on the Geology of North Africa*, pp. 1–11.
- Aubry, M.-P., Ouda, K., Dupuis, C., Berggren, W.A., Van Couvering, J.A., the Members of the Working Group on the Paleocene/Eocene Boundary, 2007. *Global Standard Stratotype – Section and Point (GSSP) for the base of the Eocene Series in the Dababiya Section (Egypt)*. *Episodes* 30 (4), 271–286.
- Bains, S., Corfield, R.M., Norris, R.D., 1999. Mechanisms of climate warming at the end of the Paleocene. *Science* 285 (5428), 724–727. <http://dx.doi.org/10.1126/science.285.5428.724>.
- Bains, S., Norris, R.D., Corfield, R.M., Faul, K.L., 2000. Termination of global warmth at the Paleocene/Eocene boundary through productivity feedback. *Nature* 407, 171–174.
- Beaumont, V., Robert, F., 1999. Nitrogen isotope ratios of kerogens in Precambrian cherts: a record of the evolution of atmosphere chemistry? *Precambrian Res.* 98, 63–82.
- Behar, F., Beaumont, V., Penteado, H.L.D., 2001. Rock-Eval 6 technology: performances and developments. *Oil Gas Sci. Technol.* 56, 111–134.
- Ben-Jacob, E., Cohen, I., Levine, H., 2000. Cooperative self-organization of microorganisms. *Adv. Phys.* 49, 395–554.
- Berggren, W.A., Ouda, K., 2003. Upper Paleocene–lower Eocene planktonic foraminiferal biostratigraphy of the Dababiya section, Upper Nile Valley (Egypt). In: Ouda, K., Aubry, M.-P. (Eds.), *The Upper Paleocene–Lower Eocene of the Upper Nile Valley: Part 1, Stratigraphy*. Micropaleontology 49, pp. 61–92 (supplement 1).
- Bertrand, P., Shimmield, G., Martinez, P., Grousset, F., Jorissen, F., Paterne, M., Pujol, C., Bouloubassi, I., Buat Menard, P., Peyrouquet, J.-P., Beaufort, L., Sicre, M.-A., Lallier-Verges, E., Foster, J.M., Ternois, Y., other participants of the Sedorqua Program, 1996. The glacial ocean productivity hypothesis: the importance of regional temporal and spatial studies. *Mar. Geol.* 130, 1–9.
- Bice, K., Marotzke, J., 2002. Could changing ocean circulation have destabilized methane hydrate at the Paleocene/Eocene boundary? *Paleoceanography* 17 (2), 2002. <http://dx.doi.org/10.1029/2001PA000678>.
- Blakey, R.C., 2007. Carboniferous–Permian paleogeography of the Assembly of Pangaea. In: Wong, Th.E. (Ed.), *Proceedings of the XVth International Congress on Carboniferous and Permian Stratigraphy*. Utrecht, 10–16 August 2003. Royal Dutch Academy of Arts and Sciences, Amsterdam, pp. 443–456.
- Bolle, M.P., Adatte, T., 2001. Paleocene–Early Eocene climatic evolution in the Tethyan realm: clay mineral evidence. *Clay Miner.* 36, 249–261.
- Bolle, M.-P., Tantawy, A.A., Pardo, A., Adatte, T., Burns, S.J., Kassab, A., 2000. Climatic and environmental changes documented in the upper Paleocene to lower Eocene of Egypt. *Ecol. Geol.* 93, 33–51.
- Bowen, G.J., Zachos, J.C., 2010. Rapid carbon sequestration at the termination of the Paleocene–Eocene Thermal Maximum. *Nat. Geosci.* 3, 866–869.
- Bowen, G.J., Koch, P.K., Gingerich, P.D., Norris, R.D., Bains, S., Corfield, R.M., 2001. Refined isotope stratigraphy across the continental Paleocene–Eocene boundary on Polecat Bench in the Northern Bighorn Basin. In: Gingerich, P.D. (Ed.), *Paleocene–Eocene stratigraphy and biotic change in the bighorn and Clarks Fork Basins, Wyoming*. 33. University of Michigan Papers on Paleontology, pp. 73–88.
- Bruland, K.W., 1983. Trace elements in sea water. In: Riey, J.P., Chester, R. (Eds.), *Chemical Oceanography* vol. 8. Academic Press, London, pp. 157–220.

- Brumsack, H.-J., 2006. The trace metal content of recent organic carbon-rich sediments: implications for Cretaceous black shale formation. *Palaeogeogr. Palaeoclimatol. Palaeoecol.* 232, 344–361.
- Campbell, I.H., Czamanske, G.K., Fedorenko, V.A., Hill, R.I., Stepanov, V., 1992. Synchronism of the Siberian traps and the Permian–Triassic boundary. *Science* 258, 1760–1763.
- Cao, Ch., Love, G.D., Hays, L.E., Wang, W., Shen, Sh., Summons, R.E., 2009. Biogeochemical evidence for euxinic oceans and ecological disturbance presaging the end-Permian mass extinction event. *Earth Planet. Sci. Lett.* 281, 188–201.
- Chamley, H., 1989. Clay sedimentology. Springer-Verlag, Berlin (623 pp.).
- Chamley, H., 1998. Clay mineral sedimentation in the Ocean. In: Paquet, H., Clauer, N. (Eds.), *Soils and sediments (mineralogy and geochemistry)*. Springer-Verlag, Berlin, pp. 269–302.
- Courtillot, V., Renne, P., 2003. On the ages of flood basalt events. *Compt. Rendus Geosci.* 335, 113–140.
- Cruse, A.M., Lyons, T.W., 2004. Trace metal records of regional paleoenvironmental variability in Pennsylvanian (Upper Carboniferous) black shales. *Chem. Geol.* 206, 319–345.
- Cullers, R.L., 2002. Implications of elemental concentrations for provenance, redox conditions, and metamorphic studies of shales and limestones near Pueblo, CO, USA. *Chem. Geol.* 191, 305–327.
- DeConto, R.M., Galeotti, S., Pagani, M., Tracy, D., Schaefer, K., Zhang, T., Pol-lard, D., Beerling, D.J., 2010. Past extreme warming events linked to massive carbon release from thawing permafrost. *Nature* 464, 87–91. <http://dx.doi.org/10.1038/nature10929>.
- Dickens, G.R., O'Neil, J.R., Rea, D.K., Owen, R.M., 1995. Dissociation of oceanic methane hydrate as a cause of the carbon isotope excursion at the end of the Paleocene. *Paleoceanography* 10, 965–971.
- Dickens, G.R., Castillo, M.M., Walker, J.C.G., 1997. A blast of gas in the latest Paleocene: simulating first-order effects of massive dissociation of oceanic methane hydrate. *Geology* 25, 259–262.
- Dickson, A., Rees-Owen, R., März, C., Coe, A., Cohen, A., Pancost, R., Taylor, K., Shcherbinina, E., 2014. The spread of marine anoxia on the northern Tethys margin during the Paleocene–Eocene Thermal Maximum. *Paleoceanography* 29, 471–488. <http://dx.doi.org/10.1002/2014PA002629>.
- Dumitrescu, M., Brassell, S.C., 2006. Compositional and isotopic characteristics of organic matter for the Early Aptian Oceanic Anoxic Event at Shatsky Rise ODP Leg 198. *Palaeogeogr. Palaeoclimatol. Palaeoecol.* 235, 168–191.
- Dupuis, C., Aubry, M.-P., Steurbaut, E., Berggren, W.A., Ouda, K., Magioncalda, R., Cramer, B.S., Kent, D.V., Speijer, R.P., Heilmann-Clausen, C., 2003. The Dababiya Quarry section: lithostratigraphy, clay mineralogy, geochemistry and paleontology. In: Ouda, K., Aubry, M.-P. (Eds.), *The Upper Paleocene–Lower Eocene of the Upper Nile Valley: Part 1. Stratigraphy*. Micropaleontology 49, pp. 41–59.
- Ernst, S.R., Guasti, E., Dupuis, C., Speijer, R.P., 2006. Environmental perturbation in the southern Tethys across the Paleocene/Eocene boundary (Dababiya, Egypt): foraminiferal and clay mineral records. *Mar. Micropaleontol.* 60 (1), 89–111.
- Espitalié, J., Deroo, G., Marquis, F., 1985. La pyrolyse Rock-Eval et ses applications. *Rev. Inst. Fr. Pétrole* 40, 563–579.
- Farrimond, P., Talbot, H.M., Watson, D.F., Schulz, L.K., Wilhelms, A., 2004. Methylhopanoids: Molecular indicators of ancient bacteria and a petroleum correlation tool. In: *Geochim. Cosmochim. Acta* 68, 3873–3882.
- Fio, K., Spangenberg, J.E., Vlahović, I., Jasenka Sremac, J., Velić, I., Ervin Mrinjek, E., 2010. Stable isotope and trace element stratigraphy across the Permian–Triassic transition: A redefinition of the boundary in the Velebit Mountain, Croatia. *Chem. Geol.* <http://dx.doi.org/10.1016/j.chemgeo.2010.09.001>.
- Gavrilov, Y.O., Shcherbinina, E.A., Oberhänsli, H., 2003. Paleocene–Eocene boundary events in the northeastern Peri-Tethys. *Geol. Soc. Am. Spec. Pap.* 369, 147–168.
- Gradstein, F.M., Ogg, J.G., Smith, A.G., Agterberg, F.P., Bleeker, W., Cooper, R.A., Davydov, V., Gibbard, P., Hinnov, L.A., House, M.R. (2), Lourens, L., Luterbacher, H.-P., McArthur, J., Melchin, M.J., Robb, L.J., Shergold, J., Villeneuve, M., Wardlaw, B.R., Ali, J., Brinkhuis, H., Hilgen, F.J., Hooker, J., Howarth, R.J., Knoll, A.H., Laskar, J., Monechi, S., Powell, J., Plumb, K.A., Raf, I., Roehl, U., Sanfilippo, A., Schmitz, B., Shackleton, N.J., Shields, G.A., Strauss, H., Van Dam, J., Veizer, J., van Kolschoten, Th. and Wilson, D. 2004. *A Geologic Time Scale 2004–2005*. Cambridge University Press, Cambridge.
- Grosjean, E., Adam, P., Connan, P., Albrecht, P., 2004. Effects of weathering on nickel and vanadyl porphyrins of a Lower Tertiary shale of the Paris basin. *Geochim. Cosmochim. Acta* 68, 789–804.
- Handley, L., Pearson, P., McMillan, I.K., Pancost, R.D., 2008. Large terrestrial and marine carbon and hydrogen isotope excursions in a new Paleocene/Eocene boundary section from Tanzania. *Earth Planet. Sci. Lett.* 275, 17–25.
- Higgins, J.A., Schrag, D.P., 2006. Beyond methane: towards a theory for the Paleocene–Eocene Thermal Maximum. *Earth Planet. Sci. Lett.* 245, 523–537.
- Holser, W.T., 1997. Geochemical events documented in inorganic carbon isotopes. *Palaeogeogr. Palaeoclimatol. Palaeoecol.* 132, 173–182.
- Huber, M., 2008. A hotter greenhouse? *Science* 321, 353–354.
- Jenkyns, H.C., 2010. Geochemistry of oceanic anoxic events. *Geochim. Geophys. Geosyst.* 11. <http://dx.doi.org/10.1029/2009GC002788> (Q03004).
- Joachimski, M.M., Ostertag-Henning, C., Pancost, R.D., Strauss, H., Freeman, K.H., Littke, R., Sinninghe Damsté, J.S., Racki, G., 2001. Water column anoxia, enhanced productivity and concomitant changes in $\delta^{13}\text{C}$ and $\delta^{34}\text{S}$ across the Frasnian–Famennian boundary (Kowala Holy Cross Mountains/Poland). *Chem. Geol.* 175, 109–131.
- Katz, M.E., Katz, D.R., Wright, J.D., Miller, K.G., Pak, D.K., Shackleton, N.J., Thomas, E., 2003. Early Cenozoic benthic foraminiferal isotopes. Species reliability and interspecies correction factors. *Paleoceanography* 18 (2), 1024.
- Keller, G., Li, L., Macleod, N., 1995. The Cretaceous/Tertiary boundary stratotype section at El Kef, Tunisia: How catastrophic was the mass extinction? *Palaeogeogr. Palaeoclimatol. Palaeoecol.* 119, 221–254.
- Kelly, D.C., Bralower, T.J., Zachos, J.C., Premoli-Silva, I., Thomas, E., 1996. Rapid diversification of planktonic foraminifera in the tropical Pacific (ODP Site 865) during the late Paleocene Thermal Maximum. *Geology* 24, 423–426.
- Kelly, D.C., Zachos, J.C., Bralower, T.J., Schellenberg, S.A., 2005. Enhanced terrestrial weathering/runoff and surface ocean carbonate production during the recovery stages of the Paleocene Eocene Thermal Maximum. *Paleoceanography* 20, 4023.
- Khozyem, H., Adatte, T., Spangenberg, J.E., Tantawy, A.A., Keller, G., 2013. Paleoenvironmental and climatic changes during the Paleocene–Eocene Thermal Maximum (PETM) at the Wadi Nukhul Section, Sinai, Egypt. *J. Geol. Soc. Lond.* 170, 341–352. <http://dx.doi.org/10.1144/jgs2012-046>.
- Khozyem, H., Adatte, T., Keller, G., Tantawy, A.A., Spangenberg, J.E., 2014. The Paleocene–Eocene GSSP at Dababiya, Egypt – Revisited. *Episodes* 37 (2), 78–86.
- Klug, H.P., Alexander, L.E., 1974. *X-ray Diffraction Procedures for Polycrystalline and amorphous Materials*. 2nd ed. John Wiley and Sons, New York.
- Knies, J., Mann, U., Popp, B.N., Stein, R., Brumsack, H.J., 2008. Surface water productivity and paleoceanographic implications in the Cenozoic Arctic Ocean. *Paleoceanography* 23. <http://dx.doi.org/10.1029/2007PA001455>.
- Kraal, P., Slomp, C.P., de Lange, G.J., 2010. Sedimentary organic carbon to phosphorus ratios as a redox proxy in Quaternary records from the Mediterranean. *Chem. Geol.* 277, 167–177.
- Kübler, B., 1987. Cristallinité de l'illite: méthode normalisées de préparation de mesure, méthode automatique normalisées de mesure. *Cahiers de l'Institut de Géologie de Neuchâtel, Series AX n°3.1 and 3.2*.
- Kuyper, M.M., Breugel, Y., Schouten, S., Erba, E., Damsté, J.S., 2004. N_2 -fixing cyanobacteria supplied nutrient N for Cretaceous oceanic anoxic events. *Geology* 32, 853–856. <http://dx.doi.org/10.1130/G20458.1>.
- Landing, W.M., Bruland, K.W., 1980. Manganese in the North Pacific. *Earth Planet. Sci. Lett.* 49, 45–46.
- Landing, W.M., Bruland, K.W., 1987. The contrasting biogeochemistry of iron and manganese in the Pacific Ocean. *Geochim. Cosmochim. Acta* 51, 29–43.
- Lu, G.Y., Keller, G., Adatte, T., Ortiz, N., Molina, E., 1996. Long-term (10^5) or short-term (10^3) $\delta^{13}\text{C}$ excursion near the Paleocene–Eocene transition: Evidence from the Tethys. *Terra Nova* 8, 347–355.
- Lu, G., Adatte, T., Keller, G., Ortiz, N., 1998. Abrupt climatic, oceanographic and ecologic changes near the Paleocene–Eocene transition in the deep Tethys basin. The Alamedilla section, southern Spain. *Ecol. Geol. Helvatica* 91, 293–306.
- Lyons, T.W., Wernicke, J.P., Hollander, D.J., Murray, R.W., 2003. Contrasting sulfur geochemistry and Fe/Al and Mo/Al ratios across the last oxic-to-anoxic transition in the Cariaco Basin, Venezuela. *Chem. Geol.* 195, 131–157.
- McInerney, F.A., Wing, S.L., 2011. The Paleocene–Eocene thermal maximum: a perturbation of carbon cycle, climate, and biosphere with implications for the future. *Annu. Rev. Earth Planet. Sci.* 39, 489–516.
- Meyers, P.A., Bernasconi, S.M., Forster, A., 2006. Origins and accumulation of organic matter in expanded Albian to Santonian black shale sequences on the Demerara Rise, South American margin. *Org. Geochem.* 37, 1816–1830.
- Millot, G., 1970. *Geology of clays*. Springer, Berlin Heidelberg New York (429 p.).
- Monechi, S., Angori, E., von Salis, K., 2000. Calcareous nannofossil turnover around the Paleocene/Eocene transition at Alamedilla (southern Spain). *Bull. Soc. Geol. Fr.* 171, 477–489.
- Murphy, A.E., Sageman, B.B., Hollander, D.J., Lyons, T.W., Brett, C.E., 2000. Black shale deposition and faunal overturn in Devonian Appalachian basin: clastic starvation, seasonal water-column mixing, and efficient biolimiting nutrient recycling. *Paleoceanography* 15, 280–291.
- Mutterlose, J., Linnert, Ch., Norris, R., 2007. Calcareous nannofossils from the Paleocene–Eocene Thermal Maximum of the equatorial Atlantic (ODP Site 1260B): evidence for tropical warming. *Mar. Micropaleontol.* 65 (1–2), 13–31.
- Nesbitt, H.W., Young, G.M., 1984. Prediction of some weathering trends of plutonic and volcanic rocks based on thermodynamic and kinetic considerations. *Geochim. Cosmochim. Acta* 48, 1523–1534.
- Nesbitt, H.W., Young, G.M., 1989. Formation and diagenesis of weathering profiles. *J. Geol.* 97, 129–147.
- Ohkouchi, N., Kawamura, K., Taira, A., 1997. Molecular paleoclimatology: reconstruction of climate variabilities in the late Quaternary. *Org. Geochem.* 27, 173–183.
- Ohkouchi, N., Kashiwaya, Y., Kuroda, J., Ogawa, N.O., Kitazato, H., 2006. The importance of diazotrophic cyanobacteria as primary producers during Cretaceous Oceanic Anoxic Event 2. *Biogeosciences* 3, 467–478.
- Olsson, R.K., Hemleben, C., Berggren, W.A., Huber, B.T., 1999. Atlas of Paleocene planktonic foraminifera. *Smithson. Contrib. Paleobiol.* 85 (I–V), 1–252.
- Pearson, P.N., Olsson, R.K., Huber, B.T., Hemleben, C., Berggren, W.A. (Eds.), 2006. Atlas of Eocene planktonic foraminifera 41. *Cushman Foundation Special Publication*, pp. 1–513.
- Perch-Nielsen, K., 1985. Mesozoic calcareous nannofossils. In: Bolli, H.H., Saunders, J.B., Perch-Nielsen, K. (Eds.), *Plankton stratigraphy*. Cambridge University Press, pp. 329–426.
- Peters, K.E., Sweeney, R.E., Kaplan, I.R., 1978. Correlation of carbon and nitrogen stable isotope ratios in sedimentary organic matter. *Limnol. Oceanogr.* 23, 598–604.
- Price, J.R., Velbel, M.A., 2003. Chemical weathering indices applied to weathering profiles developed on heterogeneous felsic metamorphic parent rocks. *Chem. Geol.* 202, 397–416.
- Pujol, F., Berner, Z., Stüben, D., 2006. Chemostratigraphy of some European Frasnian–Famennian boundary key sections. *Palaeogeogr. Palaeoclimatol. Palaeoecol.* 240, 120–145.
- Raffi, I., Backman, J., Pälike, H., 2005. Changes in calcareous nannofossil assemblage across the Paleocene/Eocene transition from the paleoequatorial Pacific Ocean. *Paleogeogr. Palaeoclimatol. Palaeoecol.* 226, 93–126.

- Renssen, H., Beets, C.J., Fichet, T., Goosse, H., Kroon, D., 2004. Modeling the climate response to a massive methane release from gas hydrates. *Paleoceanography* 19. <http://dx.doi.org/10.1029/2003PA000968>.
- Rimmer, S.M., 2004. Geochemical paleoredox indicators in the Devonian–Mississippian black shales, central Appalachian Basin (USA). *Chem. Geol.* 206 (3–4), 373–391.
- Riquier, L., Tribouillard, N., Averbuch, O., Devleeschouwer, X., Riboulleau, A., 2006. The Late Frasnian Kellwasser horizons of the Harz Mountains (Germany): two oxygen-deficient periods resulting from contrasting mechanisms. *Chem. Geol.* 233, 137–155.
- Rozsak, D.B., Colwell, R.R., 1987. Survival strategies of bacteria in the natural environment. *Microbiol. Rev.* 51 (3), 365–379.
- Sageman, B.B., Lyons, T.W., 2003. Geochemistry of fine-grained sediments and sedimentary rocks. In: Holland, H.D., Turekian, K.K. (Eds.), *Treatise on geochemistry*. Elsevier, Amsterdam (Chapter 7.06).
- Schmitz, B., Molina, E., von Salis, K., 1998. The Zumaya section in Spain: A possible global stratotype section for the Selandian and Thanetian stages. *Newsl. Stratigr.* 36, 35–42.
- Schulte, P., Scheibner, C., Speijer, R., 2011. Fluvial discharge and sea-level changes controlling black shale deposition during the Paleocene–Eocene Thermal Maximum in the Dababiya Quarry section, Egypt. *Chem. Geol.* 285, 167–183.
- Schulte, P., Schwark, L., Stassen, P., Kouwenhove, T.J., Bornemann, A., Speijer, R., 2013. Black shale formation during the Latest Danian Event and the Paleocene–Eocene Thermal Maximum in central Egypt: Two of a kind? *Palaeogeogr. Palaeoclimatol. Palaeoecol.* 371, 9–25. <http://dx.doi.org/10.1016/j.palaeo.2012.11.027>.
- Shields, G.A., Stille, P., 2001. Diagenetic constraints on the use of cerium anomalies as paleo-seawater redox proxies: an isotopic and REE study of Cambrian phosphorites. *Chem. Geol.* 175, 29–48.
- Sluijs, A., Dickens, G.R., 2012. Assessing offsets between the $\delta^{13}\text{C}$ of sedimentary components and the global exogenic carbon pool across Early Paleogene carbon cycle perturbations. *Glob. Biogeochem. Cycles* 26 (GB4005).
- Sluijs, A., Schouten, S., Pagani, M., Woltering, M., Brinkhuis, H., Sinninghe Damsté, J.S., Dickens, G.R., Huber, M., Reichert, G.J., Stein, R., 2006. Subtropical Arctic Ocean temperatures during the Paleocene/Eocene thermal maximum. *Nature* 441, 610–613.
- Sluijs, A., Brinkhuis, H., Crouch, E.M., John, C.M., Handley, L., Munsterman, D., Bohaty, S.M., Zachos, J.C., Reichert, G.-J., Schouten, S., Pancost, R.D., Sinninghe Damsté, J.S., 2008. Eustatic variations in the Paleocene–Eocene greenhouse world. *Paleoceanography* 23. <http://dx.doi.org/10.1029/2008PA001615> (PA4216).
- Soliman, M.F., Ahmed, E., Kurzweil, H., 2006. Geochemistry and mineralogy of the Paleocene/Eocene boundary at Gabal Dababiya (GSSP) and Gabal Owaina sections, Nile Valley, Egypt. *Stratigraphy* 3, 31–52.
- Spangenberg, J.E., Bagnoud-Velázquez, M., Boggiani, P.C., Gaucher, C., 2013. Redox variations and bioproductivity in the Ediacaran. Evidence from inorganic and organic geochemistry of the Corumbá Group, Brazil. *Gondwana Res.* <http://dx.doi.org/10.1016/j.gr.2013.08.014>.
- Speijer, R., Wagner, T., 2002. Sea level changes and black shales associated with the late Paleocene thermal maximum: Organic-geochemical and micropaleontologic evidence from the southern Tethyan margin (Egypt-Israel). *Geol. Soc. Am. Spec. Pap.* 356, 533–549.
- Speijer, R.P., Schmitz, B., Luger, P., 2000. Stratigraphy of late Paleocene events in the Middle East: Implications for low to middle-latitude successions and correlations. *J. Geol. Soc. Lond.* 157, 37–47.
- Srodon, J., 1999. Use of clay minerals in reconstructing geological processes: recent advances and some perspectives. *Clay Miner.* 34, 27–37.
- Storey, M., Duncan, R.A., Swisher, C.C., 2007. Paleocene–Eocene Thermal Maximum and the opening of the northeast Atlantic. *Science* 316, 587.
- Svensen, H., Planke, S., Malthes-Sorensen, A., Jamtveit, B., Myklebust, R., et al., 2004. Release of methane from a volcanic basin as a mechanism for initial Eocene global warming. *Nature* 429, 542–545.
- Svensen, H., Planke, S., Corfu, F., 2010. Zircon dating ties NE Atlantic sill emplacement to initial Eocene global warming. *J. Geol. Soc. Lond.* 167, 433–436.
- Tantawy, A.A., 2006. Calcareous nannofossils of the Paleocene–Eocene transition at Qena Region, Central Nile Valley, Egypt. *Micropaleontology* 52 (3), 193–222.
- Torstein, A., Winckler, G., Tripati, A., 2010. Productivity feedback did not terminate the Paleocene–Eocene Thermal Maximum (PETM). *Clim. Past* 6, 265–272.
- Tribouillard, N., Algeo, J., Lyons, T., Riboulleau, A., 2006. Trace metals as paleoredox and paleoproductivity proxies: An update. *Chem. Geol.* 232, 12–32.
- Weijers, J.W.H., Schouten, S., Sluijs, A., Brinkhuis, H., Sinninghe Damsté, J.S., 2007. Warm arctic continents during the Paleocene–Eocene thermal maximum. *Earth Planet. Sci. Lett.* 261, 230–238.
- Westerhold, T., Rohl, U., McCarren, H.K., Zachos, J.C., 2009. Latest on the absolute age of the Paleocene–Eocene Thermal Maximum (PETM): new insights from exact stratigraphic position of key ash layers +19 and –17. *Earth Planet. Sci. Lett.* 287, 412–419.
- Whiticar, M.J., 1999. Carbon and hydrogen isotope systematics of bacterial formation and oxidation of methane. *Chem. Geol.* 161, 291–314.
- Wignall, P.B., Newton, R., Brookfield, M.E., 2005. Pyrite framboid evidence for oxygen-poor deposition during the Permian–Triassic crisis in Kashmir. *Palaeogeogr. Palaeoclimatol. Palaeoecol.* 216, 183–188.
- Wilkin, R.T., Barnes, H.L., Brantley, S.L., 1996. The size distribution of framboidal pyrite in modern sediments: an indicator of redox conditions. *Geochim. Cosmochim. Acta* 60, 3897–3912.
- Wilkin, R.T., Arthur, M.A., Dean, W.E., 1997. History of water column anoxia in the Black Sea indicated by pyrite framboid size distributions. *Earth Planet. Sci. Lett.* 148, 517–525.
- Wing, S.L., Harrington, G.J., Bowen, G.J., Koch, P.L., 2003. Causes and consequences of globally warm climates in the Early Paleogene. In: Wing, S.L., Gingerich, P.D., Birger, S., Thomas, E. (Eds.), *Geological Society of America Special Paper*, 2003. vol. 369, pp. 425–440.
- Zachos, J.C., Kroon, D., Blum, P., et al., 2004. *Proc. ODP, Init. Repts.* Available from World Wide Web. http://www-odp.tamu.edu/publications/208_IR/208ir.htm.
- Zachos, J.C., Schouten, S., Bohaty, S., Quattlebaum, T., Sluijs, A., Brinkhuis, H., Gibbs, S., Bralower, T., 2006. Extreme warming of the mid-latitude coastal ocean during the Paleocene–Eocene Thermal Maximum: inferences from TEX86 and isotope data. *Geology* 34, 737–740.
- Zachos, J.C., Dickens, G.R., Zeebe, R.E., 2008. An early Cenozoic perspective on greenhouse warming and carbon cycle dynamics. *Nature* 451, 279–283.
- Zeebe, R.E., Zachos, J.C., Dickens, G.R., 2009. Carbon dioxide forcing alone insufficient to explain Paleocene–Eocene Thermal Maximum warming. *Nat. Geosci.* 2, 576–580.
- Zhang, Y., Lacan, F., Jeandel, C., 2008. Dissolved rare earth elements tracing lithogenic inputs over the Kerguelen Plateau (Southern Ocean). *Deep-Sea Res. II* (55), 638–652.